Grain Fragmentation and Frictional Melting During Initial Experimental Deformation and Implications for Seismic Slip at Shallow Depths

Grain fragmentation and frictional melting during initial experimental deformation and implications for seismic slip at shallow depths

Chien-Cheng Hung[1#†], Li-Wei Kuo[1*#], Elena Spagnuolo[2], Chun-Chieh Wang[3], Giulio Di Toro[2,4], Wen-Jie Wu[1], Jia-Jyun Dong[5], Wayne Lin[6], Hwo-Shuenn Sheu[3], En-Chao Yeh[7], Pei-Shan Hsieh[6]

[1]Department of Earth Sciences, National Central University, Taoyuan, Taiwan
[2]Istituto Nazionale di Geofisica e Vulcanologia, Rome, Italy
[3]National Synchrotron Radiation Research Center, Hsinchu, Taiwan
[4]Dipartimento di Geoscienze, Università di Padova, Padua, Italy
[5]Graduate Institute of Applied Geology, National Central University, Taoyuan, Taiwan
[6]Industrial Technology Research Institute, Hsinchu, Taiwan
[7]Department of Earth Sciences, National Taiwan Normal University, Taipei, Taiwan

*corresponding author
Address: No. 300, JhongDa Rd., Jhongli District, Taoyuan City 32001, Taiwan
Tel: +886-3-4227151 ext:65628 Fax: +886-3-4222044
E-mail: liweikuo@ncu.edu.tw; liweikuo@gmail.com

† now at Earth Simulation Laboratory, Department of Earth Sciences, Utrecht University, Utrecht, The Netherlands
# equal contribution

Abstract

During seismic slip, the elastic strain energy released by the wall rocks drives grain fragmentation and flash heating in the slipping zone, resulting in formation of (nano)powders and melt droplets, which lower the fault resistance. With progressive seismic slip, the frictional melt covers the slip surface and behaves as a lubricant reducing the coseismic fault strength. However, the processes associated to the transition from grain fragmentation to bulk frictional melting remain poorly understood. Here we discuss *in-situ* micro-analytical investigations performed on experimentally produced solidified frictional melts from the transition regime between grain fragmentation and frictional melting. The experiments were performed on granitic gneiss at seismic slip rates (1.3 and 5 m/s), normal stresses ranging from 3 to 30 MPa. At normal stresses < 12 MPa, the apparent friction coefficient μ_{app} (shear stress vs. normal stress) evolves in a complex manner with slip: μ_{app} decreases because of flash weakening, increases up to a peak value $\mu_{p1} \sim$ 0.6–1.0, slightly decreases and increases again to a second peak value $\mu_{p2} \sim$ 0.44–0.83, and eventually decreases with displacement to a steady-state value $\mu_{ss} \sim$ 0.3–0.45. *In-situ* synchrotron observations of the solidified frictional melt show abundance of ultra-fine quartz grains before μ_{p2} and enrichment in SiO_2 at μ_{p2}. Because partial melting occurs on the ultra-fine quartz grains and, as a consequence, it suggested that the second re-strengthening (μ_{p2}) is induced by the higher viscosity of the melt due to its enrichment in Si from melting of the ultra-fine quartz grains derived from grain fragmentation.

Keyword: frictional melting, grain fragmentation, ultrafine quartz, viscosity, synchrotron analysis.

1. Introduction

Numerous physical and chemical processes have been theoretically and experimentally proposed to justify fault lubrication during seismic slip, for example, flash heating (Rice, 2006; Beeler et al., 2008; Goldsby and Tullis, 2011), powder lubrication (Han et al., 2010; Reches and Lockner, 2010), frictional melting (Spray, 2005; Di Toro et al., 2006a), silica gel formation (Di Toro et al., 2004), elastohydrodynamic lubrication (Brodsky and Kanamori, 2001; Cornelio et al., 2019), grain size- and temperature-dependent processes (Green et al., 2015; De Paola et al., 2015; Spagnuolo et al., 2015; Rowe et al., 2019) and thermal decomposition (Han et al., 2007; Collettini et al., 2013). In particular, on a fault patch in silicate-built rocks, flash heating and melting (Goldsby and Tullis, 2011) or grain fragmentation of the rock (Green et al., 2015; De Paola et al., 2015; Spagnuolo et al., 2015; Rowe et al., 2019; Chen et al., 2017a) may occur during the initial stages of seismic slip at the passage of the earthquake rupture propagation front. With progressive slip, the continuously generated melt droplets can accumulate to form a continuous melt layer possibly resulting in melt lubrication (Spray, 1995; Hirose and Shimamoto, 2005). Therefore, studies on powder generation, flash heating and melting, and the formation of a continuous melt layer provided criteria for understanding fault lubrication (Reches and Lockner, 2010; Chen et al., 2017a; Spray, 1995; 2005; Di Toro et al., 2006; Rice, 2006; Beeler et al., 2008; Goldsby and Tullis, 2011).

However, the transition between fault rock comminution and frictional melting remains unclear. More relevantly, how do the associated frictional properties derived from both fault comminution and frictional melting affect the fault strength during fault rupture is not well-constrained. Here, we address these questions by conducting rock friction experiments on granitic gneiss at seismic rates and further discuss how the presence of fragmented grains and the chemical evolution of the friction melt influence the frictional behavior of the experimental fault.

2. Materials and Methods

2.1 Starting materials

The exhumed pseudotachylyte-bearing fault, which crosscuts the granitic gneiss of the Tananao Metamorphic Complex (TMC), crops out in the Hoping area, northeast Taiwan (Chu et al., 2012; Fig. 1a). The fault zone rocks are mainly cataclasites and mylonites overprinted by pseudotachylytes. Pseudotachylytes were generated at depths > 4 km about 1.6 Ma ago (Chen et al., 2017) in faults accommodating displacements by up to 220 mm (corresponding to earthquakes of M_W 6.4 ± 0.4 if all the displacement would be associated to a single seismic slip event; Korren et al., 2015). Pseudotachylytes form vein and injection veins networks that intrude the host

granitic gneiss, and they were used to infer earthquake source parameters (e.g., slip vectors, Korren et al., 2015; brushlines, Ferré et al., 2016). We used the granitic gneiss from the Hoping borehole cores drilled by the Industrial Technology Research Institute (ITRI) as the starting materials for the rotary shear experiments (Fig. 1b and 1c). The mineral composition of the core granitic gneiss is 35–40% quartz, 15–25% feldspar, 20–25% micas (muscovite dominant) and 5–10% other accessory minerals (estimated by optical microscope analysis of thin sections). This estimated composition is similar to the modal content of the granitic gneiss cropping out in the area with 30–35% quartz, 20–25% feldspar, 30–35% micas (both muscovite and biotite), 3–5% clinozoisite-epidote and titanite, as well as 2% of other accessory minerals (Chu et al., 2012). The bulk chemical composition of the granitic gneiss is also shown in Table 1. The granitic gneiss has a heterogeneous mineralogical distribution due to the presence of a foliation enriched in muscovite or in quartz and feldspar (Fig. 1b and 1c). To achieve more homogenous mineralogy of the sliding surface, the samples prepared for the experiments were drilled with the long axis oblique (approximately 25° to 30°) to the gneissic foliation.

2.2 Rock deformation experiments

Rock deformation experiments were conducted with the low-to-high velocity rotary shear friction apparatus (LHVR) installed at the National Central University (NCU), Taiwan (Yang et al., 2014; Kuo et al., 2015), and the slow-to-high velocity apparatus (SHIVA) at the Istituto Nazionale di Geofisica e Vulcanologia (INGV, Rome), Italy (Di Toro et al., 2010). The latter was used to extend the applied normal stresses up to 30 MPa and perform an experiment under vacuum conditions.

For LHVR, the samples were solid cylinders (25 mm external diameter) which were tightly confined with iron wires (Fig. 1b). For SHIVA, the samples were hollow cylinders (50 mm external, 30 mm internal diameters) which were jacketed with an external aluminum ring (Fig. 1c; Niemeijer et al., 2011; Nielsen et al., 2012). To improve the alignment of two mounted samples before the experiments, for LHVR, we gently knocked the edge of the upper one until the measured un-centered degree was lower than 10 μm, and, for SHIVA, we pre-ground the slip surface of the samples at 1 cm/s and 1 MPa (Niemeijer et al., 2011). The pre-grinding lasted until the recorded torque achieved a constant value which is associated with the parallelism of the two opposite sliding surfaces.

Because of the rotary configuration of the two machines used, both slip and slip rate increase with sample radius. As a consequence, we define the equivalent slip rate V_e (Shimamoto and Tsutsumi, 1994; Hirose and Shimamoto, 2005):

$$V_e = \frac{4\pi R(r_{ext}^2 + r_{ext}r_{int} + r_{ext}^2)}{3\,(r_{ext} + r_{int})}\ [\frac{m}{s}] \qquad \text{Eq. 1}$$

where R is the revolution rate of the motor (i.e., the target R in the experiments presented here were 1500 rpm for LHVR and 3000 rpm for SHIVA), r_{ext} the external radius (12.5 and 25 mm for LHVR and SHIVA, respectively), and r_{int} the internal radius (0 mm and 15 mm for LHVR and SHIVA, respectively) of the samples (Fig. 1). The experimental conditions above resulted in target V_e of 1.3 m/s and 5 m/s for LHVR and SHIVA, respectively. Hereafter we refer to the "equivalent slip rate" as slip rate. The measured torque (T) allows us to determine the shear stress (τ) by assuming that τ is constant over the entire slip surface (Hirose and Shimamoto, 2005):

$$T = \int_{r_{int}}^{r_{ext}} 2\pi\tau r^2 dr = \frac{2\pi\tau}{3}(r_{ext}^3 - r_{int}^3)\ [N\ m] \qquad \text{Eq. 2}$$

Given the strong assumption of a constant shear stress over the entire slip surface, which cannot be the case as the shear stress varies with slip rate (e.g., Di Toro et al., 2011) and in the cylindrical configuration the slip rate increases with the sample radius, mechanical data obtained with hollow cylinders are more accurate than those obtained with solid cylinders. From Eq. 2, the friction coefficient μ is:

$$\mu = \frac{\tau}{\sigma} = \frac{3T}{2\pi\sigma(r_{ext}^3 - r_{int}^3)} \qquad \text{Eq. 3}$$

hereafter we refer to μ as apparent friction coefficient μ_{app} for the following description.

The LHVR experiments were conducted at normal stresses of 3, 6, 9, 12, and 19 MPa, at a target slip rate of 1.3 m/s, and under room humidity conditions. The SHIVA experiments were conducted at the normal stresses of 3 and 30 MPa, respectively, and at a target slip rate of 5 m/s under both vacuum and room humidity conditions (Table 2). All mechanical data (torque, angular rotation, and axial displacement) were acquired at a frequency up to 1 kHz and 25 kHz for LHVR and SHIVA, respectively. The friction coefficient of the granitic gneiss evolved in a complex manner with slip. Because of this, we conducted slip-stepping experiments or experiments that were stopped at the about the maximum or minimum values of the friction coefficient.

2.3 Analytical methods

1. We impregnated the experimental products of LHVR with epoxy resin and prepared petrographic thin sections and rock slices, both cut across the diameter of the sample and perpendicular to slipping surface. The petrographic thin sections were prepared with a thickness of 30 μm, mounted on silica glass and polished by 0.3 μm thick alumina powder for optical and scanning electron microscopy analysis. The thickness of rock slices were ~ 1 mm for *in-situ* synchrotron X-ray diffraction (XRD) and micro-Raman spectroscopy analysis.
2. Three-lens optical microscopy (OM) (Leica DMLP) coupled with an image

capture system, and field emission scanning electron microscopy, coupled with an energy dispersive spectrometer (FESEM/EDX) (JSM-7000F model) equipped at the National Central University, Taiwan, were used to investigate the microstructures and determine the semi-quantitative chemical composition of the solidified frictional melt. For SEM-EDX, the petrographic sections were sputtered with platinum at 5 nm thickness and semi-quantitatively analyzed at 15 kV with a focused beam of ~ 1 μm in diameter.

3. The *in-situ* synchrotron XRD installed at the beamline BL01C2 in the National Synchrotron Radiation Research Center (NSRRC), Taiwan, was used to determine the mineral assemblages of both the solidified frictional melt and the host rock. The analyses were operated at a wavelength of 0.774910 Å, with an electron beam energy of 1.5 GeV and a beam size of 150 μm in diameter. Because of the presence of large grains (~ 1.0 mm in size) of quartz, the samples of gneiss, differently from the solidified frictional melts, were reduced into powders and analyzed. This prevented the presence of intensity anomalies in the XRD spectra due to the occurrence of crystals (e.g., quartz) larger than the X-ray beam (Kuo et al., 2014a, b). However, the intensity anomalies can still be observed in the results of the glass matrix owing to the presence of large survivor quartz or feldspar grains. To reduce the effect of intensity anomalies and representatively present the synchrotron XRD data, the spectra were reported as the average values of three analyses on the same sample.
4. The micro-Raman spectroscopy (Horiba Jobin Yvon UV–VIS Labram HR) at the National Taiwan Museum was used to determine the presence of water within the solidified frictional melt. We focused on the region from 100 to 4,000 cm^{-1} on the Raman spectrum. The analysis was operated with a 532 nm laser as an excitation source with a beam size of 1−2 μm in diameter under a ×100 objective with a final laser power of 100 mW on the sample surface. A charged-coupled device (CCD) detector was installed in the microscope used to focus the excitation laser beam to collect the backscattered Raman signal. We collected three data of the matrix per deformed sample for the solidified frictional melt at an acquisition time of 15 s per analysis. We added the Raman spectra of pure water and quartz for comparison.
5. The synchrotron transmission X-ray microscopy (TXM) at the beamline BL01B1 (Song et al., 2007a, b; Yin et al., 2006) at the NSRRC, Taiwan, was used to obtain X-ray radiographies to determine the particle size distribution (PSD) of the survivor clasts hosted in the solidified frictional melt. The analysis was conducted on a 30-μm-thick sample collected from the petrographic thin sections

over an area of 375 μm x 75 μm. The beam X-ray energy was 8 keV and the analysis had a spatial resolution of 50-nm (see Song et al., 2007a, b).

6. The software *ImageJ* (available at https://imagej.nih.gov/ij/) was used to process the images of both the back scattering electron (BSE) and the TXM to estimate the PSD of the survivor grains within the solidified frictional melt. *ImageJ* allowed us to measure the size of quartz grains by exploiting the gray contrast between the glass matrix and the quartz grains in the BSE images (Kuo et al., 2015). On the contrary, we draw by hand the survivor grains from the TXM images due to the difficulty of the contrast identification between glass matrix and grains. By doing this, the overlapping of the survivor grains could be also clearly identified.
7. One experiment (LHVR1097) performed on granitic gneiss from the outcrop was recorded with an infrared thermal-sensing camera (thermoIMAGER TIM160, MICRO-EPSILON) to measure the temperature evolution of the experimental fault with slip. The infrared camera, integrated with the TIMConnect software, provided an instantaneous measurement of the temperature from 150°C to 900°C over an area of 0.6 mm in diameter at an acquisition rate of 10-500 Hz. Since the slipping zone is < 0.3 mm in thickness and the temperature is measured from outside, the measured temperatures yielded a minimum estimate of the temperatures achieved in the slipping zone.

3. Results

3.1 Frictional behavior and temperature evolution during fast shear experiments

The mechanical data exhibit a complicated evolution of μ_{app} with slip, which varied with normal stress (Fig. 2a). At slip initiation, once the static friction μ_s was overcome, μ_{app} decreased rapidly to a first minimum value (possibly associated with flash heating and weakening, see discussion). Then the frictional evolution varied with normal stress:

At large normal stresses (≥ 12 MPa, e.g., experiment s1289, Fig. 2a) μ_{app} increased to a peak value $\mu_{p1} = 0.66$ and then dramatically decreased to a low value of 0.16 ± 0.01 (an average value of friction coefficient after peak friction and before the sample was broken) defined in the literature as steady state friction μ_{ss} (e.g., Di Toro et al., 2011). At the end of slip, during sample deceleration, μ_{app} increased again. In general, this frictional evolution with slip is consistent with previous experiments performed on silicate-built cohesive rocks sheared at seismic slip rates (Hirose and Shimamoto, 2005; Di Toro et al., 2006a, b; Niemeijer et al., 2011; Passelègue et al., 2016).

At low normal stresses (< 12 MPa, e.g., experiments LHVR 0438 and

LHVR0452, Fig. 2a and 3), after slip initiation and initial flash weakening, μ_{app} first increased to a peak value at μ_{p1}~1.0, then decreased to 0.8-0.5, then increased again to a second peak value at μ_{p2} ~ 0.44–0.83 and eventually decreased with displacement to μ_{ss} ~ 0.3 ± 0.01–0.45 ± 0.08. Then, similarly to the large normal stress experiments, μ_{app} increased again at the end of slip (Fig. 2a). This complicated evolution, though observed in previous experiments, has been only partly discussed (e.g., Hirose and Shimamoto, 2005; Di Toro et al., 2006).

With the aim of investigating the process responsible for the μ_{p1} and μ_{p2}, we analyzed the slipping zone produced in dedicated experiments stopped, with increasing slip (slip-stepping experiments, Fig. 3), after:

(1) 1.5 m of slip corresponding to μ_{p1} (State A, experiment LHVR0487);

(2) 2.6 m of slip corresponding to the frictional strength decrease between μ_{p1} and μ_{p2} (State B, experiment LHVR0534);

(3) 2.1 m of slip corresponding to ca. μ_{p2} (State C, experiment LHVR0452);

(4) 5.7 m of slip during the final weakening (State D, "steady-state" conditions, experiment LHVR0438).

To illustrate the temperature evolution with slip for loading conditions identical to those imposed in the reference experiment LHVR0438 where "steady-state" conditions were achieved, experiment LHVR1097 was equipped with an infrared thermal-sensing camera. Because the emissivity ε of melt varies with temperature, we set two values of ε, 0.55 and 0.9 for high and low temperature, respectively (Abtahi et al., 2002). For ε = 0.55, the temperature of the slipping zone immediately increased to ~430°C (ca. 0.6 m of slip in Fig. 3e), slightly rose to ~500°C at State A (ca. 1.2 m of slip), slightly decreased and remained a constant value of ~450°C during State B (between 1.2 and 2 m of slip), steadily rose to ~750°C at State C (between 2 and 3 m of slip), and eventually increased to a constant value of ~850°C during State D (from 3 m to the end of slip). There was a loss of temperature measurements (between ~3.5 to 4 m of slip) because of connection issues with the infrared camera. For ε = 0.9, with respect to the estimated temperatures for ε = 0.55, temperatures achieved in the different States were lower by about ~100°C for States A and B, ~200°C for State C and ~250°C for State D.

Regarding the entire experimental dataset, the initial peak (corresponding to μ_{p1}) and steady-state (corresponding to μ_{ss}) shear stress increased linearly with normal stress, resulting in an effective friction coefficient of ~0.3 and ~0.11 for μ_{p1} and μ_{ss}, respectively (Fig. 2b). Instead, the second μ_{p2} disappeared with increasing normal stress (Fig. 2a).

3.2 Microstructures, mineralogy and chemical composition of the solidified

frictional melt

We recovered the experimental products of the slip-stepping experiments and investigated with OM, FESEM-EDX, synchrotron XRD and synchrotron TXM. The mineralogy and microstructures of the slipping zones are shown in Figures 4, 5, and 6. In general, the thickness of the experimental slipping zones increases from the edge (were the slip rate is the highest) to the center (were the slip rate is nominally zero) of the circular slip surface (Fig. 4a to d). In the experiment stopped at State A, the solidified melt patches were discontinuous and meniscus-shaped (Fig. 4). In the experiments stopped at states B and C, the solidified melt formed a continuous and dark-coloured donut-shaped feature. In the experiment stopped at State D, the solidified melt covered the entire slip surface (Fig. 4). In addition, the boundary solidified melt / host rock was irregular (presence of embayments, indicated by arrows in Figs. 4a-d) due to selective melting of the low-melting-point minerals (e.g., muscovite) of the granitic gneiss (see Hirose and Shimamoto, 2003; Fig. 4d). The average thickness of the solidified frictional melt layers was determined by averaging the value of the real melt thickness obtained at different horizontal positions of the solidified melt on the slip surface. Although this measurement might result in an underestimate value as it includes the extrusion of melt at the end of slip, the melt thickness still notably varied at each state from ~ 270 μm in State A, ~ 330 μm in State B, ~ 170 μm in State C, and ~ 230 μm in State D (Table 2).

The *in-situ* synchrotron XRD data show that the mineral assemblage of the host rock (black line) was composed of quartz, feldspar, calcite, and muscovite (Fig. 4e). Instead, the clasts suspended in the solidified frictional melts produced in the slip-stepping experiments were mainly composed of quartz and minor feldspar (Fig.4e). As observed in both natural and experimental pseudotachylytes, this indicates that quartz is more resistant than feldspar and muscovite during comminution and melting (see Spray, 2010, for a review). Unfortunately, the signals of the presence of amorphous materials (= glass matrix of the pseudotachylytes) between 15° to 40° of 2θ were not detected in the synchrotron XRD spectra because of the strong signal depression due to the high peaks of quartz.

Under the FESEM-BSE, the grains of the undeformed Hoping granitic gneiss are angular and elongated in shape, with grain size varying from ~0.1 to ~1.0 mm (not shown). The representative BSE images of the solidified melts under identical magnification show a substantial amount of sub-angular quartz grains and the presence of vesicles distributed within the glass matrix (Fig. 5). It is clear that the grain size distribution of the survivor grains of quartz varies significantly over the four states of the slip-stepping experiments, e.g., grains < 5 μm in size in State C are more abundant than in both States B and D (Fig. 5 and section 3.5).

The TXM images show the overlapping of rounded to sub-rounded survivor grains which ranged from 50 nm to 10 μm in diameter within the solidified melts representative of the four states of the slip-stepping experiments (Fig. 6). For grains < 5 μm (size range that is difficult to be clearly observed under SEM-BSE), we find that the shapes of the survivor grains in the TXM images were in rounded or spherical shape, similar occurrence to the survivor quartz grains reported from Kuo et al. (2015). These results suggest that partial melting on the edge of grains likely occurred, in particular, for ultra-fine grains (Kuo et al., 2015).

We utilized FESEM/EDS to analyze the matrix of the solidified frictional melts and adopted the average value of 40 points as representative of the chemical composition of the matrix (Table 1). The analysis showed no significant chemical variation of the composition of the solidified frictional melts from any of the four states of the slip-stepping experiments, except for the enrichment in SiO_2-content from State A to State C and particular high CaO-content in State D. The Raman spectra of the slip-stepping experiments showed negligible water content in the solidified frictional melts (Fig. 7).

3.3 Frictional melt viscosity and temperature estimate

In addition to the measured temperature of the frictional melt during the experiment LHVR1097, we also estimated the possible viscosity and temperature of the friction melt in the four states following the method suggested by Wallace et al. (2019). The non-Arrhenian Newtonian temperature-dependence viscosity of the silicate melt can be estimated by the GRD viscosity calculator (available online at https://www.eoas.ubc.ca/~krussell/VISCOSITY/grdViscosity.html) by inputting the melt composition (table 1; Giordano et al., 2008; Lavallée et al., 2012). This calculation is based on the Vogel-Fulcher-Tamman equation:

$$Log\,\eta = A + \frac{B}{T(K) - C} \qquad \text{Eq. 5}$$

where the η is viscosity (Pa s), A, B, and C, are the modelled parameters based on viscosity measurement of geochemical composition (Giordano et al., 2008), and T the silicate melt temperature (K). We obtained the viscosity curves for the slip-stepping frictional melts (Fig. 8) by giving at the constant A the value of -4.55 (optimal value based on Giordano et al. (2008)), and the values of B and C were obtained from the chemical composition of the glasses and 17 adjustable parameters (see demonstration calculation in Giordano et al. (2008), Table 1). The presence of vesicles suggests that some volatiles (e.g., OH from muscovite) were present in the melt, but the water content in the glass was likely negligible and assumed to be zero based on the absence of water signal from Raman analysis (Fig. 7).

Based on the mechanical data, the apparent viscosity of the frictional melts (η_{app}) can be directly calculated by the ratio of the measured shear stress to the strain rate as:

$$\eta_{app} = \frac{\tau}{\dot{\varepsilon}} = \frac{\tau w}{V_e}\ [Pa\ s] \quad \text{Eq.6}$$

where τ is the measured shear stress (Pa), $\dot{\varepsilon}$ is the strain rate (s^{-1}), w is the thickness of the melt layer (an underestimate of the thickness during sliding as it includes the extrusion of melt at the end of slip) and V_e is the equivalent slip velocity (m/s). Because solid particles (= survivor clasts) are present in the frictional melts, the calculated apparent viscosity could be overestimated (e.g., Metzner, 1985). To correct the effect of clasts on the apparent viscosity, we calculated the relative viscosity (η_r) using an empirical equation (Kitano et al., 1981):

$$\eta_r = (1 - \frac{\phi}{A})^{-2} \quad \text{Eq. 7}$$

with $A = 0.54–0.0125r$, where ϕ is the volume fraction (volume particles/total volume) of the clasts, A is the parameter related to the packing geometry of the solid particles and r is the average aspect ratio of solid grains (about 2 in our case). We measured the ϕ using BSE images from the center to the edge of the experimental pseudotachylyte and averaged the value. The value of ϕ ranged from ~0.11 at State C to ~0.20 at State A, B, and D (Table 2). Moreover, the presence of vesicles should lower the apparent viscosity of the frictional melt (e.g. Manga et al., 1998). However, the volume fraction of the vesicles is small (< 0.1) and shows no significant variation in the four states. Therefore, the contribution of the vesicles to the apparent viscosity should be negligible (Lejeune et al., 1999). Based on Eqs. 6 and 7, the mechanically-constraint apparent viscosities corrected with the presence of clasts ($\eta_c = \eta_{app} / \eta_r$) are ~229 Pa s at State A, ~232 Pa s at State B, ~125 Pa s at State C, and ~99 Pa s at State D (Table 2).

According to the model for Non-Arrhenian temperature-dependence of melt viscosity (Eqs. 5; Wallace et al., 2019), the chemically- and mechanically-constraint apparent viscosities for the four states are consistent with the temperature of ~1370°C (State A), ~1300°C (State B), ~1456°C (State C), and ~1265°C (State D) (Fig. 8). These chemo-mechanical-constraint temperature estimates are at odds with the temperature measured estimated with the infrared camera, as it will be discussed in section 4.3.

3.4 Particle size distribution (PSD)

The PSD was obtained by measuring all clasts (mainly made of quartz) within

the solidified frictional melt from the images of both SEM and TXM. With the FESEM, for each state, we collected eight to twelve BSE contiguous images to cover almost entirely slipping zone. Moreover, we collected some images at higher magnification (1,300X, similar to Fig. 5) to obtain more accurate size distribution on finer grains (< 10 μm). With the TXM, for each state, we analyzed identical areas of 375 μm in length and 75 μm in width, corresponding to the central part of the slipping zone. Since the TXM images included all the grains over the entire thickness (30 μm) of the thin-section, the number of particles measured from the TXM images has different unit compared to that from BSE images (i.e. number of particles per μm^2 for SEM and per μm^3 for TXM). Therefore, we further divided the obtained data from the TXM images by the sample thickness (μm) to integrate it with the PSD data from the BSE images. To increase the accuracy of the density data in size range of 1–3 μm (lower limit of SEM analysis), we extend the TXM results to overlap this size range. The density data in this overlapping range is reported as the average value of both TXM and SEM results.

The PSD data were plotted as a cumulative frequency diagram for the mean diameter, r, using a logarithmic scale. Our results (solid dots) were fitted and plotted with solid curves for mean diameters > 1 μm and as dashed lines for diameters < 1 μm. The particle density, $N(r)$, which represents the cumulative number of particles per μm^2, follows a function of mean diameter (r), defined as the geometric mean of the major and minor axes of an irregular grain, in the form of a power-law for frictional melting (not comminution): $N(r) = N'(1 + r/r')^{-D}$, where N is the cumulative number of grain sizes greater than r, that is, N' (which depends on the total number of measurements), r' is constant, and D is the fractal dimension (Shimamoto and Nagahama, 1992; Tsutsumi, 1999).

The fitted curves for each state are almost identical, i.e., the curves are steep in the coarse-grained size ranges (> 10 μm) and gently flatten towards fine size < 10 μm, and to some degree the PSDs obey to a power-law (Fig. 9). Interestingly, we find that the measured particle density for the grain sizes smaller than 1 μm is larger than the fitted curves, in particular, at states A and B (Fig. 9). Based on the previous PSD studies of the experimentally produced pseudotachylytes, the slope of the PSD curves shows a linearly steep to horizontal evolution in the size range from about 100 μm to 0.5 μm (e.g. Tsutusmi, 1999, Fig. 2). These curves were obtained from the solidified melt with long displacement experiments (hundreds of meters) and the change of the slope was suggested to be the effect of partial melting of the survivor grains. Therefore, compared to our results obtained from the short-displacement experimental melt (< 3 m), the deviation between measured density data and fitted curves in size <

1 μm, particularly significant in States A and B, may suggest that the ultra-fine quartz grains derived from the surface comminution are trapped in the melts. Instead, the PSD of the clasts from State C is described by a larger value for *D*. The reduced thickness of the slipping zone during frictional melting is one of the factors controlling the size reduction of the clasts in the coarse-grained range and, as a consequence, the fractal dimension of their distribution (Tsutsumi, 1999). In addition, thickness of the melt zone might strongly depend on the viscosity and thus on the temperature of the melt layer. This may suggest the high value of *D* at State C might be controlled by the melt thickness (the thinnest among the slip-stepping experiments). But here we cannot evaluate how the size reduction and melt viscosity influence the *D* value due to their complicated correlation and more comprehensive studies are required.

4. Discussion

4.1 Frictional evolution during fast fault slip at low normal stress

We focus on the complicated frictional evolution of granitic melts at low normal stress. Chen et al. (2017b) performed frictional experiments on granitic rocks for moderate velocities (0.01–0.11 m/s) to investigate the complicated frictional evolution with slip at the transition between powder lubrication and melt lubrication. They suggested that the evolution of the frictional behavior can be divided into three stages based on different physical mechanisms: the initial weakening stage (Stage 1: powder lubrication), the initial strengthening stage (Stage 2: viscous melt patches), and the final weakening stage (Stage 3: melt lubrication) (Fig. 10a). They concluded that this complicated frictional evolution is the result of thermally-activated deformation processes. In the discussion below, we exploit the conceptual model proposed by Chen et al. (2017b) to our experimental dataset. At slip initiation, during Stage 1, we propose that flash heating and melting of the asperity contacts is the dominant weakening mechanism once a threshold sliding velocity of > 0.1 m/s (case for silicate-built rocks) is achieved (Rice, 2006; Di Toro et al., 2006b; Hirose and Shimamoto, 2005; Niemeijer et al., 2011; Goldsby and Tullis, 2011; Proctor et al., 2014; Violay et al., 2014a; Fig. 10b-e). Then, we divide the Stage 2 of Chen et al. (2017b) (dynamic fault strengthening in the presence of powders and melt patches) into States A (first peak), B, and C (second peak) and keep Stage 3 of Chen et al. 2017b (weakening due to the presence of a continuous melt layer) as our State D (see also discussion in Hirose and Shimamoto, 2005; Di Toro et al., 2006b; Niemeijer et al., 2011; Violay et al., 2014b; Proctor et al., 2014) (Fig. 10b-e). Below we focus on the complex frictional evolution during Stage 2.

459 **4.2 Initial strengthening in Stage 2 (State A)**

460 At slip initiation, when flash heating occurs, temperatures significantly rise at the
461 asperity scale and melt the rock contacts (Rice, 2006). In addition, rubbing of the
462 asperity contacts induces tribo-chemical reactions and triggers different mechanisms.
463 Therefore, tribo-chemical reactions may occur at lower activation energies (and thus
464 their kinetics is more efficient at a given temperature) than thermo-chemical reactions
465 (Steinike and Tkácová, 2000). It is reasonable to assume that flash heating of the
466 granitic gneiss may result in the preferential fusion of the low melting point minerals
467 (i.e., muscovite, T_m = 650°C–900°C at 1 atm; Spray, 2010, see discussion below) but
468 also in the formation of silica-rich melt droplets from fusion of high melting point
469 minerals as quartz (main mineral of the gneiss, T_m = 1720°C at 1 atm; Spray, 2010).
470 The melt patches in State A were derived from the accumulation of the melt droplets
471 produced by flash heating and melting at the asperity contacts, resulting in the
472 formation of relatively silica-rich melts.

473 In addition, the PSD data of State A shows the presence of ultra-fine grains,
474 suggesting an additional source of grains into the melt. When frictional melts
475 occurred and covered the entire slip surface, the survivor grains were mainly derived
476 from thermal cracking and frictional melting of the wall rocks and sticking out from
477 the wall rocks into the melt. Based on this, compared to the PSD of State D, we
478 conclude that the additive grains in State A were the result of mixtures of rock clasts
479 (by rock fragmentation) and melt patches during initial sliding.

480 The temperature measured with the infrared camera at State A is ~500°C, and it
481 is likely an underestimated because of (1) averaging with the slipping zone and the
482 wall-rocks and (2) slightly unfocused measuring (outside of the slipping zone).
483 Integrated with the mineralogical observation (Fig. 4e), the temperature at State A
484 should achieve the breakdown point of muscovite (at least > 650°C) and was
485 relatively lower than the other states (with shorter slip and less frictional work input;
486 see the details in section 4.3). Therefore, the estimated temperature and corresponding
487 viscosity (Fig. 8 and Table 1) indicate that the silica-rich melt patches of State A were
488 highly viscous and presumably contributed to the resistance of shearing, resulting in
489 the initial strengthening in Stage 2, similar to the observation reported by Chen et al.
490 (2017b).

491

492 **4.3 Re-strengthening in Stage 2 (states B to C)**

493 With progressive sliding, the melt patches accumulated into a donut-shaped melt
494 layer and the two rock specimen were partly separated from the melt layer (States A to
495 B; Fig. 4b). Here, we simply neglect the contribution from solid-solid friction in the
496 central part of the slip surface because the torque and thus the shear stress increase

with sample radius (e.g., Eq. 2), where the frictional contribution from the inner part of the cylinder is negligible (Hirose and Shimamoto et al., 2005). In addition, because the microstructural observation shows that solidified melts were thicker than the surface roughness (Fig. 4), the solid-solid contacts at the outer melt regime were unlikely to have occurred. We suggest that donut-shape melt layer is the main contribution for shear resistance during the experiment. As a consequence, melt viscosity and shear strain rate are the dominant parameters that control the shear resistance of the simulated fault during the frictional melting regime (States B to D).

Melt viscosity is controlled by three parameters: temperature, presence of water, and chemical composition (Lejeune et al., 1999; Fluegel et al., 2004). According to the mechanically-constraint viscosity model (section 3.3), the temperatures achieved in States A to D are about 1370˚C, 1300˚C, 1456˚C, and 1265˚C, respectively (Fig. 8). The estimated temperature of State D (melt lubrication regime) is in good agreement with previous rock friction experiments conducted at seismic slip rates (Hirose & Shimamoto, 2005; Di Toro et al., 2006; Niemeijer et al., 2011, 2012; Nielsen et al., 2008). The estimated temperature of State D (1265˚C) can be set as the upper bound for the temperature achieved in the slip-stepping experiments. In fact, the temperature achieved in States A to C should be lower than the one achieved during State D because, under the same conditions, the shorter slip also imply less work input by the motor. Therefore, according to the evaluation of temperature at State D, the estimated temperature of State C (1456˚C) is overestimated.

On the basis of the mineralogy of the survivor clasts (e.g., muscovite was melted through all the slip-stepping experiments; Fig. 4e), we can take the melting point of muscovite into consideration to estimate the temperature of the friction melt. The melting point (T_m) of muscovite during static heating at a low heating rate of 1˚C/min is 650˚C (Spray, 2010) and T_m increases to 900 ˚C at a high heating rate of 200 ˚C/min (Kuo et al., 2011). Because of the difficulty of evaluating on one side the contribution of grinding processes during frictional sliding that may further lower the T_m of muscovite and, on the other side the heating rate which is much higher than the aforementioned heating rates tested in the laboratory (e.g., Kuo et al., 2011), we assume that the lower bound of the temperature achieved during States B and C is ~900˚C.

In experiment LHVR1097 we measured the temperature evolution from States A to D (Fig. 3e). The temperature measured by the infrared camera is affected by (1) absorption (i) of emitted radiance by gases produced during frictional sliding (SO_2, H_2O, CO_2) and (ii) of the powders suspended in the air, (2) variance of emissivity (ε), and (3) the thickness of the slipping zone which is thinner than the area investigated by the infrared camera (i.e., the camera measures the temperature over an area that

includes both the hot slipping zone and the cold wall rocks). As a consequence, the temperature measured with the infrared camera is commonly considered as an underestimated value. Abtahi et al. (2002) reported that broadband emissivity systematically rises as the lava cools, from 0.55 at 1050°C to 0.85 at <500°C. In our case, the widespread preferential melting of muscovite demonstrates that temperatures were higher than 650˚C in the slipping zones of States A to D. As a consequence, it seems that a low value of emissivity ($\varepsilon = 0.55$) is more appropriate for the temperature measurements with the infrared camera, and thus, the associated estimated temperature is ~850˚C, as the lower bound of temperature of States B and C. Taken together, the achieved temperatures for States A to C should be in the range of 850˚C to 1265˚C (the pink area in Fig. 8).

In the temperature range of 850˚C to 1265˚C, the viscosity of the melt in State C is higher than the one achieved in the other states ($10^{8.0}$–$10^{3.1}$ Pa s, $10^{7.7}$ –$10^{2.7}$ Pa s, $10^{8.2}$ –$10^{3.3}$ Pa s for States A to C, respectively). In addition, the slope of the Non-Arrhenian temperature dependence of the viscosity curves become less steep. This suggests that even if the temperature of the melt increases with slip between States B and C (i.e. temperature at State C is slightly higher than the one at State B; Fig. 3e), the estimated viscosity at State C can be higher than the one at State B.

To summarize, because of frictional heating, the bulk temperature in the slipping zone increases with slip (Fig. 3e) and likely reduces the melt viscosity, resulting in melt lubrication (Di Toro et al., 2006). However, by itself, the gradual temperature increase, which would result in less viscous friction melts, is at odds with the re-strengthening behavior (i.e., μ_{p2} occurred at an higher temperature than μ_{p1}; Figs. 2 and 3e). On the basis of the temperature-viscosity model (Fig. 8), the evolution of the chemical composition of the frictional melt with slip might be the most plausible explanation for re-strengthening from State B to C. Though water was present at the initiation of slip (the experiments were performed under room-humidity conditions) and released by the breakdown of muscovite, because of the not-confined conditions, gases could escape from the frictional melt. This resulted in the formation of vesicles and in the negligible water content of the pseudotachylyte matrix (Raman spectroscopy data in Fig. 7). As a consequence, water cannot be responsible for the variation of the viscosity of the melt in any of the States. On the other hand, the experiment s1286 under vacuum conditions (Table 1) may further indicate the re-strengthening is irrelevant to the humidity and/or oxidation. Taken together, the increase in SiO_2 in the frictional melt might be the most plausible contributor for the re-strengthening from State B to State C (Table 1).

The presence of clasts made of quartz and, to a less extent, feldspar and the absence of muscovite in the solidified frictional melt (Figs. 4e, 5) suggest that

573 selective melting of low-melting-point minerals (i.e., muscovite) took place (Shand,
574 1916; Sibson, 1975; Spray, 1987). However, the chemical composition of the glass
575 matrix at States B and C is higher in SiO_2 and lower in CaO (Table 1) compared to the
576 composition of the glass matrix at State D which was produced at higher temperatures
577 (Fig. 3e). This chemical variation suggests that partial melting of quartz was more
578 efficient at States B and C than State D while partial melting of feldspar was
579 comparatively efficient at State D. In fact, during State D the sliding surfaces were
580 entirely separated by the frictional melt (Fig. 4d) and grain fragmentation due to
581 solid-solid contact of the asperities was less efficient than during States A to C.
582 Therefore, the presence of rock powders (mostly made by quartz and feldspar) in the
583 frictional melts likely drove further melting of the small grains by quasi-equilibrium
584 melting (Lee et al., 2017) or by the Gibbs-Thomson effect due to the high
585 surface-to-area ratio (Hirose and Shimamoto, 2003). These particular melting
586 processes resulted in the increase of Ca (although not obvious in our result) and
587 especially Si content in the frictional melt and, as a consequence, in the increase of
588 the melt viscosity from State B to State C (Table 1). Without the addition of
589 fragmentation products, the chemical composition of the glass matrix at State D was
590 then mainly derived from the melting of feldspar and muscovite.
591 We propose that the enrichment in Si in the frictional melt associated to
592 grain-by-grain fragmentation at the initiation of simulated seismic slip may explain
593 the observed fault re-strengthening observed in previous experiments performed at
594 seismic rates (Di Toro et al., 2006b; Hirose and Shimamoto, 2005; Niemeijer et al.,
595 2011) (Fig. 10). Moreover, this process of chemical evolution of melt composition
596 with slip also support the model proposed by Fialko and Khazan (2005) according to
597 which thermal-activated slip strengthening is likely to occur in quartz-rich rocks at
598 shallow depths.
599
600 **4.4 Final weakening during Stage 3 (State C to D)**
601 The final fault weakening is observed in all the experiments, but of course not in
602 the short slip-stepping experiments (Fig. 2b), and is associated to the formation of a
603 continuous frictional melt layer (Fig. 4d). In fact, frictional melts with high
604 temperatures and low silica content (Table 1) are an efficient lubricant, consistently
605 with previous experimental and theoretical studies (Hirose & Shimamoto, 2005; Di
606 Toro et al., 2006a, b; Niemeijer et al., 2011, 2012; Nielsen et al., 2008). In addition,
607 our mechanical data are comparable to those of previous experiments on tonalite
608 (similar mineral assemblages without foliation) where both data show low effective
609 friction coefficient (0.13 and 0.05, respectively) at the steady-state melting (Di Toro et
610 al., 2006a, b). This suggests that the mineralogical heterogeneity of the specimens due

611 to the metamorphic foliation makes only a very minor influence on the obtained
612 values of shear stress.
613
614 **4.5 Rock friction experiments and Re-strengthening behavior**
615 The mechanical data shows a complicated evolution of the friction coefficient
616 (flash weakening, first strengthening, slight weakening, second strengthening, and
617 eventually weakening) with slip at low normal stresses (< 10 MPa) (Fig. 2a). This
618 complicated evolution almost disappears and approximates an exponential decay at
619 larger normal stresses (e.g., 30 MPa) (Fig. 2a). The most significant change with
620 increasing normal stress is the reduction of the first peak value μ_{p1} and the
621 disappearance of the second peak μ_{p2} (Fig. 2a). This is the result of the more
622 continuous transition from flash weakening to melt lubrication with increasing normal
623 stress, but also with increasing slip rate and slip acceleration rate (5 m/s and 6.5 m/s^2,
624 respectively, for the experiments performed with SHIVA). In fact, the higher heat
625 production rate, proportional to the product of the normal stress per slip rate,
626 dissipated on the slipping zone results in the fast generation of the frictional melt and
627 rapid reduction of the friction coefficient. Therefore, at larger normal stresses and slip
628 rates, the effect of surface comminution becomes negligible during the onset of slip.
629 In the case of the experiments performed with SHIVA, sample preparation
630 (pre-grounding process) can influence the frictional evolution with slip. Niemeijer et
631 al. (2011) pre-grounded the samples with SHIVA to achieve perfect alignment and
632 obtained a complicated friction evolution afterward. It seems that, by doing this,
633 ultra-fine powders were likely generated and potentially stuck on the asperities of the
634 slip surface, even though the powder was cleaned with an air brush before the
635 high-speed experiment. Nielsen et al. (2012) applied a new method to align the
636 SHIVA samples without pre-grinding the slip surfaces and obtained a simpler
637 evolution (which approximated an exponential decay) of the friction coefficient at slip
638 initiation (Violay et al., 2014a,b; Violay et al., 2019). Therefore, both SHIVA and
639 LHVR results demonstrate the presence of a correlation between the presence of
640 fragments in the slipping zone and the second re-strengthening behavior.
641
642 **4.6 Implications for natural Hoping pseudotachylyte**
643 We apply our experimental results to the natural observations of the Hoping
644 pseudotachylyte. Ferré et al. (2016) proposed to use a novel linear structure
645 decorating the slip surfaces of pseudotachylytes, described as "brushlines", to identify
646 the coseismic slip direction. The brushlines were suggested to form through viscous
647 brushing between protruding asperities of the host rocks and the viscous frictional
648 melt (solid-liquid interaction) during rapid cooling at the end of slip. The chemical

compositions of the Hoping pseudotachylyte (average 61% silica content, Kuo, 2016) and of the experimental pseudotachylytes from the same rocks generated in State C (Table 1) are very similar. It implies that the Hoping pseudotachylyte likely formed during small seismic slip events or at the initial fault sliding (corresponding to State B to C) and contained remnant grains from fault comminution. If so, our finding about the chemically induced increased viscosity of the frictional melt might be another explanation for the process of viscous brushing.

5. Conclusions

In this study, we present the mechanical results of slip-stepping experiments performed on solid cylinders of granitic gneisses sheared at high slip velocities using rotary shear machines (SHIVA and LHVR) coupled with high-resolution microstructural (scanning electron microscope, Transmission X-ray microscopy, image analysis, etc.) and mineralogical (synchrotron X-ray diffraction analysis, micro-Raman spectroscopy, etc.) investigations of the experimental fault products. In the case of the experiments performed at seismic slip rates (1.3 to 5 m/s) but low normal stress (< 10 MPa), the mechanical data show a complicated frictional evolution with slip which includes: initial weakening, first strengthening followed by a slight decrease and then by a second strengthening and a final exponential decay towards a steady state value (Figs. 2-3). This complex frictional evolution becomes less pronounced in the experiments performed at larger normal stresses and is associated with the evolution of the viscosity of the frictional melts (chemical composition, temperature, etc.) (Figs. 4-9 and Table 1). We thus modified the model of Chen et al. (2017b) for the various friction behaviors (stages 1 to 3) associated with different physical mechanisms (Fig. 10). We propose that the initial fault weakening is due to the grain fragmentation and flash heating and weakening on bare rock surfaces. The first fault strengthening is due to braking from the formation of a highly viscous (also because of the low temperature) frictional melt. The second fault re-strengthening is associated with the increased viscosity mainly because of the SiO_2 enrichment of the frictional melt. The increase in SiO_2 content is probably due by a combination of quasi-equilibrium melting and the Gibbs-Thomson effect on the ultra-fine quartz grains. The final weakening is due to melt lubrication because of the formation of a continuous melt layer covering the entire slip surface together with the reduction of the viscosity because of the increased temperature of the melt.

Considering the experimental conditions at which the chemically-induced high viscosity frictional melt forms, we suggest that the surging of frictional melts generated behind the rupture front likely hampers seismic slip during initial earthquake propagation at shallow depths, even though melt lubrication takes place

afterward. As a natural example, although the Hoping pseudotachylytes were generated at depths > 4km, our result suggests that the chemically-induced high viscosity frictional melt formed in the Hoping area may therefore play a braking role during fault rupture into shallow depths.

Acknowledgements

This research was supported by the European Research Council Consolidator Starting Grant 614705 NOFEAR to Giulio Di Toro and Taiwan ROC (Republic of China) Ministry of Science and Technology (MOST 108-2116-M-008-021-MY2) to Li-Wei Kuo. Samples were prepared by Jialiang Si via the National Science Foundation of China (41572192, 41330211). We thank Taiwan Power Company and Industrial Technology Research Institute for providing the Hoping borehole cores, and Dr. Che-Ming Yang and Hsiu-Ching Hsiao for their laboratory support. The experimental data supporting this work are publicly available online (http://140.115.20.219:5000/sharing/VTj4nVZcU).

References cited

Abtahi, A.A., Kahle, A.B., Abbot, E.A., Gillespie, A.R., Sabol, D., Yamada, G., and Pieri, D.C. (2002), Emissivity changes in basalt cooling after eruption from Pu'u O'o [abs.]: Eos (Transactions, American Geophysical Union), 83, no. V71A-1263.

Beeler, N., T. Tullis, and D. Goldsby (2008), Constitutive relationships and physical basis of fault strength due to flash heating, J. Geophys. Res., 113, B01401, doi:10.1029/2007JB004988.

Brodsky, E. E. and Kanamori, H. (2001), Elastohydrodynamic lubrication of faults. J. Geophys. Res. 106, 16,357–16,374, doi: 10.1029/2001JB000430.

Bürgmann, R., and G. Dresen (2008), Rheology of the lower crust and upper mantle: Evidence from rock mechanics, geodesy, and field observations, Annual Review of Earth and Planetary Sciences, v. 36, p. 531–567, doi: 10 .1146 /annurev .earth .36 .031207 .124326.

Byerlee, J. (1978), Friction of rocks, Pure Appl. Geophys., 116, 615–626, doi: 10.1007/BF00876528.

Carslaw, H., and J. Jaeger (1959), Conduction of Heat in Solids, vol. 19591, Clarendon Press, Oxford, doi: 10.1007/978-1-4939-2565-0_2.

Chen, X., A. S. E. Madden, and Z. Reches (2017a), Powder-rolling as a mechanism of dynamic fault weakening, In M. Thomas, T. Mitchell, & H. Bhat (Eds.), Fault zone dynamic processes: Evolution of fault properties during seismic rupture (pp. 133–150). Washington, DC and Hoboken, NJ: American Geophysical Union and

John Wiley, doi: 10.1002/9781119156895.ch7.

Chen, X., A. S. E. Madden, and Z. Reches (2017b), Friction evolution of granitic faults: heating controlled transition from powder lubrication to frictional melt, J. Geophys. Res., doi: 10.1002/2017JB014462.

Chen, C.-T., C.-Y. Wu, C.-H. Lo, H.-T. Chu, and T.-F. Yui (2017), Dating palaeo-seismic faulting in the Taiwan Mountain Belt, Terra Nova, v. 30, issue 2, doi: 10.1111/ter.12319.

Chu, H.-T., S.-L. Hwang, P. Shen, and T.-F. Yui (2012), Pseudotachylyte in the Tananao Metamorphic Complex, Taiwan: Occurrence and dynamic phase changes of fossil earthquakes, Tectonophysics, v. 581, p. 62–75, doi: 10 .1016/j .tecto .2012 .01 .017.

Collettini, C., C. Viti, T. Tesei, and S. Mollo (2013), Thermal decomposition along natural faults during earthquakes, Geology, 41, 923–930. doi:10.1130/G34421.1.

Cornelio, C., E. Spagnuolo, G. Di Toro, S. Nielsen and M. Violay (2019), Mechanical behavior of fluid-lubricated faults, Nature Communications, 10:1274, doi: 10.1038/s41467-019-09293-9.

De Paola, N., Holdsworth, R.E., Viti, C., Collettini, C., Bullock, R., (2015), Can grain size sensitive flow lubricate faults during the initial stages of earthquake propagation? Earth Planet. Sci. Lett. 431, 48–58, doi: org /10 .1016 /j .epsl .2015 .09 .002.

Di Toro, G., D. L. Goldsby, and T. E. Tullis (2004), Friction falls towards zero in quartz rock as slip velocity approaches seismic rates, Nature, 427, 436–439, doi: 10.1038/nature02249.

Di Toro, G., G. Pennacchioni, and G. Teza (2005), Can pseudotachylytes be used to infer earthquake source parameters? An example of limitations in the study of exhumed faults, Tectonophysics, 402, 3–20, doi: 10.1016/j.tecto.2004.10.014.

Di Toro, G., T. Hirose, S. Nielsen, G. Pennacchioni, and T. Shimamoto (2006a), Natural and experimental evidence of melt lubrication of faults during earthquakes, Science, 331, 647–649, doi: 10.1126/science.1121012.

Di Toro, G., T. Hirose, S. Nielsen, and T. Shimamoto (2006b), Relating high-velocity rock-friction experiments to coseismic slip in the presence of melts, in Radiated Energy and the Physics of Earthquake Faulting, Geophys. Monogr. Ser., vol. 170, edited by R. Abercrombie et al., pp. 121–134, AGU, Washington, D. C., doi: 10.1029/170GM13.

Di Toro, G., A. Niemeijer, A. Tripoli, S. Nielsen, F. Di Felice, P. Scarlato, G. Spada, R. Alessandroni, G. Romeo, G. Di Stefano, S. Smith, E. Spagnuolo, and S. Mariano (2010), From field geology to earthquake simulation: a new state-of-the-art tool to investigate rock friction during the seismic cycle (SHIVA), Rendiconti Lincei,

763 1–20, doi: 10.1007/s12210-010-0097-x.
764 Ferré, E. C., E.-C. Yeh, Y.-M. Chou, R.-L. Kuo, H.-T. Chu, and C. S. Korren (2016),
765 Brushlines in fault pseudotachylytes: a new criterion for coseismic slip direction,
766 Geology 44 (5), 395–398, doi:10.1130/G37751.1.
767 Fialko, Y., and Y. Khazan (2005), Fusion by earthquake fault friction: Stick or slip?, J.
768 Geophys. Res., 110, B12407, doi:10.1029/2005JB003869.
769 Giordano, D., J. K. Russell, and D. B. Dingwell (2008), Viscosity of magmatic liquids:
770 a model, Earth and Planetary Science Letters 271, 123–134, doi:
771 10.1016/j.epsl.2008.03.038.
772 Goldsby, D. L., and T. E. Tullis (2011), Flash heating leads to low frictional strength
773 of crustal rocks at earthquake slip rates, Science, 334, 216–218, doi:
774 10.1126/science.1207902.
775 Green, H. W., F. Shi, K. Bozhilov, G. Xia, and Z. Reches, (2015), Phase
776 transformation and nanometric flow cause extreme weakening during fault slip,
777 Nat. Geosci., 8, 448–489, doi: 10.1038/ngeo2436
778 Han, R., T. Shimamoto, T., Hirose, J.-H. Ree and J. Ando (2007), Ultralow friction of
779 carbonate faults caused by thermal decomposition, Science 316 (5826), 878–881,
780 doi: 10.1126/science.1139763.
781 Han, R., T. Hirose, , and T. Shimamoto (2010). Strong velocity weakening and
782 powder lubrication of simulated carbonate faults at seismic slip rates. J. .Geophys.
783 Res., 115, B03412, doi: 10.1029/2008JB006136.
784 Hayashi, N. and A. Tsutsumi (2010), Deformation textures and mechanical behavior
785 of a hydrated amorphous silica formed along an experimentally produced fault in
786 chert, Geophys. Res. Lett. 37, L12305, doi: 10.1029/2010GL042943.
787 Hirose, T., and T. Shimamoto (2003), Fractal dimension of molten surfaces as a
788 possible parameter to infer the slip-weakening distance of faults from natural
789 pseudotachylites, J. Struct. Geol., 25, 1569–1574, doi:
790 10.1016/S0191-8141(03)00009-9.
791 Hirose, T., and T. Shimamoto (2005), Growth of molten zone as a mechanism of slip
792 weakening of simulated faults in gabbro during frictional melting, J. Geophys.
793 Res., 110, B05202, doi: 10.1029/2004JB003207.
794 Kitano, T., T. Kataoka, and T. Shirota (1981), An empirical equation of the relative
795 viscosity of polymer melts filled with various inorganic fillers, Rheol. Acta, 20,
796 207–209, doi: 10.1007/BF01513064.
797 Korren, C. S., E. C. Ferré, E.-C. Yeh, Y.-M. Chou and H.-T. Chu (2016), Seismic
798 rupture parameters deduced from a Pliocene fault pseudotachylyte in Taiwan, In
799 M. Y. Thomas, T. M. Mitchell, and H. S. Bhat (Eds.), Fault Zone Dynamic
800 Processes: Evolution of Fault Zone Properties and Dynamic Processes During

801 Seismic Rupture AGU Monograph, (p. 227). Washington, USA: American
802 Geophysical Union, doi: 10.1002/9781119156895.ch2.
803 Kuo, L.-W., S.-R. Song, L. Huang, E.-C. Yeh and H.-F. Chen (2011), Temperature
804 estimates of coseismic heating in clay-rich fault gouges, the Chelungpu fault
805 zones, Taiwan, Tectonophysics, 502, 315–327, doi: 10.1016/j.tecto.2011.02.001.
806 Kuo, L.-W., H. Li, S. Smith, G. Di Toro, J. Suppe, S. R. Song, S. Nielsen, H. S. Sheu
807 and J. Si (2014a), Gouge graphitization and dynamic fault weakening during the
808 2008 Mw 7.9 Wenchuan earthquake, Geology 42, 47–50, doi: 10.1130/G34862.1.
809 Kuo, L.-W., H. C. Hsiao, S.-R. Song, H. S. Sheu and J. Suppe (2014b), Coseismic
810 thickness of principal slip zone from the Taiwan Chelungpu fault Drilling
811 Project-A (TCDP-A) and correlated fracture energy, Tectonophysics, 619–620,
812 29-35, doi: 10.1016/j.tecto.2013.07.006.
813 Kuo, L.-W., Y.-F. Song, C.-M. Yang, S.-R. Song, C.-C. Wang, J.-J. Dong, J. Suppe,
814 and T. Shimamoto (2015), Ultrafine spherical quartz formation during seismic
815 fault slip: Natural and experimental evidence and its implications, Tectonophysics,
816 664, 98–108, doi: 10.1016/j.tecto.2015.09.008.
817 Kuo, R.-L. (2016). Microstructural and Magnetic Investigations of Pseudotachylyte
818 and Ultracataclasite in the Hoping River, Tananao Complex, Eastern Taiwan.
819 Unpubl. M.Sc. thesis, National Taiwan University, Taipei, Taiwan, R.O.C.
820 Lavallée, Y., T. M. Mitchell, M. J. Heap, J. Vasseur, K.-U. Hess, T. Hirose and D. B.
821 Dingwell (2012), Experimental generation of volcanic pseudotachylyte:
822 constraining rheology, J. Struct. Geol. 38, 222–233, doi:
823 10.1016/j.jsg.2012.02.001.
824 Lee, S. K., R. Han, E. J. Kim, G. Y. Jeong, H. Khim and T. Hirose (2017),
825 Quasi-equilibrium melting of quartzite upon extreme friction, Nature Geoscience,
826 10, 436–441, doi: 10.1038/ngeo2951.
827 Lejeune, A. M., Bottinga, Y., Trull, T. W., Richet, P. (1999), Rheology of
828 bubble-bearing magmas, Earth Planet. Sci. Lett. 166, 71–84, doi:
829 10.1016/S0012-821X(98)00278-7.
830 Lin, A. and T. Shimamoto (1998), Selective melting processes as inferred from
831 experimentally generated pseudotachylytes, J. Asian Earth Sci., 16, 533–545, doi:
832 10.1016/S0743-9547(98)00040-3.
833 Lin, A (2008), Fossil earthquakes: The formation and preservation of
834 pseudotachylytes, Berlin Heidelberg: Springer-Verlag, doi:
835 10.1007/978-3-540-74236-4.
836 Manga, M., J. Castro, K. V. Cashman, and M. Loewenberg (1998), Rheology of
837 bubble-bearing magmas, J. Volcanol. Geotherm. Res., 87, 15– 28, doi:
838 10.1016/S0377-0273(98)00091-2.

839 Metzner, A. B. (1985), Rheology of suspensions in polymeric liquids, J. Rheol., 29,
840 739–775, doi: 10.1122/1.549808.
841 Nielsen, S., G. Di Toro, T. Hirose, and T. Shimamoto (2008), Frictional melt and
842 seismic slip, J. Geophys. Res., v. 113, no. B01308, doi: 10.1029/2007JB005122.
843 Nielsen, S., E. Spagnuolo, and M. Violay (2012), The ultimate sample preparation for
844 rotary shear experiments. Rapporti tecnici INGV,
845 (http://istituto.ingv.it/l-ingv/produzione-scientifica/rapporti-tecnici-ingv/numeri-p
846 ubblicati-2012).
847 Niemeijer, A., G. Di Toro, S. Nielsen, and F. Di Felice (2011), Frictional melting of
848 gabbro under extreme experimental conditions of normal stress, acceleration, and
849 sliding velocity, J. Geophys. Res., 116, B07404, doi: 10.1029/2010JB008181.
850 Niemeijer, A., G. Di Toro, W. A. Griffith, A. Bistacchi, S. A. Smith, and S. Nielsen
851 (2012), Inferring earthquake physics and chemistry using an integrated field and
852 laboratory approach, J. Struct. Geol., 39, 2–36, doi: 10.1016/j.jsg.2012.02.018.
853 Passelègue, F. X., E. Spagnuolo, M. Violay, S. Nielsen, G. Di Toro and A. Schubnel
854 (2016), Frictional evolution, acoustic emissions activity, and off-fault damage in
855 simulated faults sheared at seismic slip rates, J. Geophys. Res., 121, 7490–7513,
856 doi: 10.1002/2016JB012988.
857 Proctor, B.P., Mitchell, T.M., Hirth, G., Goldsby, D., Zorzi, F., Platt, J.D., and Di Toro,
858 G. (2014), Dynamic weakening of serpentinite gouges and bare surfaces at
859 seismic slip rates: Journal of Geophysical Research, v. 119, doi: 10 .1002
860 /2014JB011057.
861 Reches, Z., and D. A. Lockner (2010), Fault weakening and earthquake instability by
862 powder lubrication, Nature, 467, 452–455, doi: 10.1038/nature09348.
863 Rice, J. R (2006), Heating and weakening of faults during earthquake slip, J. Geophys.
864 Res., 111, B05311, doi: 10.1029/2005JB004006.
865 Rowe, C., K. Lamothe, M. Rempe, M. Andrews, T. Mitchell, G. Di Toro, J. Clancy
866 White and S. Aretusini (2019), Earthquake lubrication and healing explained by
867 amorphous nanosilica, Nature Communications, 10, 320, doi:
868 10.1038/s41467-018-08238-y.
869 Shand, S. J. (1916), The pseudotachylyte of Parys, Geol. Soc. London Quart. Jour. 72,
870 198–221.
871 Shimamoto, T. and H. Nagahama (1992), An argument against the crush origin of
872 pseudotachylytes based on the analysis of clast-size distribution, J. Struct. Geol.,
873 14, 999–1006, doi: 10.1016/0191-8141(92)90031-Q.
874 Shimamoto, T. and A. Tsutsumi, (1994). A new rotary-shear high-speed frictional
875 testing machine: Its basic design and scope of research, J. Tectonic Res. Group of
876 Japan, 39, 65–78 (in Japanese with English abstract).

877 Sibson, R. H (1975), Generation of pseudotachylyte by ancient seismic faulting.
878 Geophysical Journal International, 43(3), 775–794, doi:
879 10.1111/j.1365-246X.1975.tb06195.x.
880 Song, S. R., L. W. Kuo, E. C. Yeh, C. Y. Wang, J. H. Hung, and K. F. Ma (2007a),
881 Characteristics of the lithology, fault-related rocks and fault zone structures in
882 the TCDP Hole-A, Terr. Atmos. Ocean. Sci. 18, 243–269, doi:
883 10.3319/TAO.2007.18.2.243(TCDP).
884 Song, Y. -F., et al. (2007b), X-ray beamlines for structural studies at the NSRRC
885 superconducting wavelength shifter, J. Synchrotron Radiat. 14, 320–325, doi:
886 10.1107/S0909049507021516.
887 Spagnuolo, E., Plümper, O., Violay, M., Cavallo, A., Di Toro, G., 2015. Fast-moving
888 dislocations trigger flash weakening in carbonate-bearing faults during
889 earthquakes. Sci. Rep.5, 1–11. https://doi .org /10 .1038 /srep16112.
890 Spray, J. G. (1987), Artificial generation of pseudotachylyte using friction welding
891 apparatus: Simulation of melting on a fault plane, J. Struct. Geol., 9, 49–60, doi:
892 10.1016/0191-8141(87)90043-5.
893 Spray, J. G. (1992), A physical basis for the frictional melting of some rock-forming
894 minerals, Tectonophysics, 204, 205–221, doi: 10.1016/0040-1951(92)90308-S.
895 Spray, J. G. (1993), Viscosity determinations of some frictionally generated silicate
896 melts: Implications for fault zone rheology at high strain rates, J. Geophys. Res.,
897 v. 98, p. 8053–8068, doi: 10 .1029 /93JB00020.
898 Spray, J. G. (1995), Pseudotachylyte controversy: fact or friction. Geology, 23, 1119–
899 1122, doi: 10.1130/0091-7613(1995)023<1119:PCFOF>2.3.CO;2.
900 Spray, J. G. (2005), Evidence for melt lubrication during large earthquakes, Geophys.
901 Res. Lett., 32, L07301, doi: 10.1029/2004GL022293.
902 Spray, J.G. (2010), Frictional melting processes in planetary materials: from
903 hyper-velocity impacts to earthquakes. Annu. Rev. Earth Planet. Sci.38, 221–254,
904 doi: org /10 .1146 /annurev.earth .031208 .100045.
905 Steinike, U. and K. Tkáčová (2000), Mechanochemistry of Solids—Real Structure
906 and Reactivity, Journal of Materials Synthesis and Processing, 8, 197, doi:
907 10.1023/A:1011364110355.
908 Tsutsumi, A. and T. Shimamoto (1997), High-velocity frictional properties of gabbro,
909 Geophys. Res. Lett., 24, 699–702, doi: 10.1029/97GL00503.
910 Tsutsumi, A. (1999), Size distribution of clasts in experimentally produced
911 pseudotachylytes, J. Struct. Geol., 21, 305–312, doi:
912 10.1016/S0191-8141(98)00113-8.
913 Violay, M., G. Di Toro, S. Nielsen, B. Gibert, E. Spagnuolo, P. Azais, and P. G.
914 Scarlato, (2014a), Effect of glass on the frictional behavior of basalts at seismic

slip rates, Geophys. Res. Lett., 41, 348–355, doi: 10.1002/2013GL058601.
Violay, M., S. Nielsen, B. Gibert, E. Spagnuolo, A. Cavallo, P. Azais, , S. Vinciguerra, and G. Di Toro (2014b), Effect of water on the frictional behavior of cohesive rocks during earthquakes. Geology, 42 (1), 27–30.
Violay, M., F. Passelegue, E. Spagnuolo, G. Di Toro and C. Cornelio (2019), Effect of water and rock composition on re-strengthening of cohesive faults during the deceleration phase of seismic slip pulses, Earth and Planetary Sciences, 522, 55–64, doi: 10.1016/j.epsl.2019.06.027.
Wallace, P. A., S. H. De Angelis, A. J. Hornby, J. E. Kendrick, S. Clesham, F. W. von Aulock, A. Hughes, J. E. P. Utley, T. Hirose, D. B. Dingwell, and Y. Lavallé (2019), Frictional melt homogenisation during fault slip: Geochemical, textural and rheological fingerprints, Geochimica et Cosmochimica Acta, 255, 265–288, doi: 10.1016/j.gca.2019.04.010.
Yang, C. H., W.-L. Yu, J.-J. Dong, C.-Y. Kuo, T. Shimamoto, C.-T. Lee, T. Togo, and Y. Miyamoto (2014), Initiation, movement, and run-out of the giant Tsaoling landslide — what can we learn from a simple rigid block model and a velocity–displacement dependent friction law? Eng. Geol., 182, 158–181, doi: 10.1016/j.enggeo.2014.08.008.
Yin, G.-C., Y.-F. Song, M.-T. Tang, F.-R. Chen, K. S. Liang, F. W. Duewer, M. Feser, W. Yun and H.-P. D. Shieh (2006), 30 nm resolution X-ray imaging at 8 keV using third order diffraction of a zone plate lens objective in a transmission microscope, Appl. Phys. Lett., 89, doi:10.1063/1.2397483.

Captions

Figure 1. (a) Geological setting of the Hoping area with complex tectonic structures. The inset box shows the location of the Hoping area in northeast Taiwan. The study area consists mainly of marble, granitic gneiss, and schist. The Hoping pseudotachylyte (red star) and its surface structure "brushlines" (green box; the surface was coated by Pt for SEM analysis) and the Hoping borehole are located alongside the Hoping River and are hosted in granitic gneiss. The attitude of foliation is mostly parallel or sub-parallel to the direction of fold axis. (b, c) Specimen assembly for LHVR and SHIVA. Note that the specimen size for LHVR is 25 mm in diameter and for SHIVA, the outer diameter is 50 mm and the inner diameter is 30 mm. Specimens were bound with iron wires and jacketed with aluminum rings for LHVR and SHIVA, respectively.

Figure 2. Mechanical and compiled data from experiments performed with LHVR and SHIVA machines. (a) Apparent friction coefficient as a function of displacement

under normal stresses from 3 to 30 MPa and slip velocity at 1.3 m/s (LHVR) and 5 m/s (SHIVA) under room humidity (LHVR) and vacuum (SHIVA) conditions. The static friction, initial weakening, first peak and second peak are indicated by the arrows. (b) Shear stress of the first peak (red circle), second peak (blue diamond), and steady-state value (black square) varied with normal stress. Note that the dynamic shear strength for peak states and steady state is well below Byerlee′s friction values ($0.6 < \mu < 0.85$).

Figure 3. Evolution of the apparent friction coefficient, slip velocity, axial displacement and temperature with displacement of five slip-stepping experiments. (A) State A (LHVR0487) stopped at the peak value representing the first slip-strengthening behavior. (B) State B (LHVR0534) was stopped at the second slip-weakening behavior. (C) State C (LHVR0452) stopped at the second slip-strengthening behavior. (D) State D (LHVR0438) was stopped at the steady-state value. (E) The experiment reproducing the condition of LHVR0438 with outcrop sample coupled with the infrared thermal-sensing camera. The temperature increases with slip from 150°C (minimum detected value of the infrared camera) at the slip of ~0.4 m to ~850°C ($\varepsilon = 0.55$) and ~600°C ($\varepsilon = 0.9$) at the slip of ~5.3m.

Figure 4. Experimental results of four states with corresponding schematic sketch of the solidified frictional melt distribution on the slip surface. The petrographic sections were prepared to be perpendicular to the slip surface and analyzed from half-way from the center to the edge. (a–d) Open Nicol observation of the experimental products. The frictional melt distribution evolves from the melt patches in State A, to a donut-shape melt layer in State B (5x intensity for compare) and C, to a fully covered melt layer in State D, respectively. (e) In situ synchrotron XRD analysis of the host rock and the experimental products from the simulated fault surface. The disappearance of the diffraction peak of mica and reduction of the diffraction intensity of feldspar and quartz are reflected in the XRD spectra and show no variation between the four states. The different colors between the melt spectra are indicated by the calculated bulk temperature where the red line refers to a higher melting temperature than the pink lines.

Figure 5. BSE images of the frictional melts for four states. (a) In State A, quartz grains (dark grey) with sizes ranging from 2 to 10 μm are abundant within the melt matrix (light grey). For (b), State B, the number of quartz grains with a size lower than 5 μm decreased. For (c), State C, smaller quartz grains (< 1 μm) appeared while larger quartz grains (> 10 μm) disappeared. For (d), State D, quartz grains with sizes

991 larger than 10 μm are dominant within the melt. The dark area with spherical to
992 ellipsoidal occurrence are vesicles, which are particularly larger in State D.
993
994 Figure 6. TXM images of the solidified frictional melts for the four states. Internal
995 microstructures all show substantial ultrafine quartz grains with sub-angular and
996 angular-to-spherical, and ellipsoidal surrounded by a melt matrix. (a) The enlarged
997 image highlights the appearance of the fractured grains. (b) The enlarged image
998 highlights the overlapping occurrence of ultrafine spherical quartz. (c) The enlarged
999 image shows no distinct boundary of ultrafine quartz with a sub-angular to the
1000 spherical shape. (d) The enlarged image shows a distinct occurrence of ultrafine
1001 spherical to ellipsoidal quartz.
1002
1003 Figure 7. Representative Raman spectra of the glass from four states, quartz, and
1004 water. The signal for the presence of water is barely observed for each state.
1005
1006 Figure 8. Non-Arrhenian temperature dependence of viscosity for four states. The
1007 viscosity curves were derived using the GRD viscosity model of the Giordano et al.
1008 (2008) based on the chemical composition of the glass matrix. The apparent viscosity
1009 corrected with clast content (η_c) was derived from the mechanical data. Intersection
1010 points are the estimates of temperature of chemo-mechanical data for the four states.
1011 The temperatures achieved for states A to C were estimated between the achieved
1012 temperature of State D and the melting point of muscovite obtained by slow heating
1013 (650°C) and fast heating rate (900°C) experiments. See the main text for further
1014 discussion. Two temperatures obtained by infrared measurement from emissivity (ε)
1015 of 0.55 and 0.9 were plotted.
1016
1017 Figure 9. Particle size distribution of surviving grains within the melt matrix for four
1018 states. Cumulative particle density as a function of mean diameter. The particle
1019 density, $N(r)$ representing the cumulative number of particles per μm^2, following a
1020 function of particle mean diameter (r) in micrometers with regression lines (solid lines)
1021 in a form of power law $N(r) = N'(1 + r/r')^{-D}$. The obtained particle density from TXM
1022 analyses is relatively higher than the interpolated regression line (dashed line) for the
1023 four states.
1024
1025 Figure 10. Frictional evolution with displacement for crystalline silicate rocks. (a)
1026 Schematic sketch of the frictional evolution of Sierra white granite sheared at a slip
1027 velocity of 0.048 m/s under a normal stress of 1.22 MPa (after Chen et al., 2017b).
1028 The associated slipping mechanisms corresponding to each stage were shown. (b)

Indian Gabbro sheared at a slip velocity of 0.85 m/s under a normal stress of 1.5 MPa (after Hirose and Shimamoto, 2005). (c) South Africa gabbro sheared at a slip velocity of 3 m/s under a normal stress of 20 MPa (after Niemeijer et al., 2012). (d) Tonalite sheared at a slip velocity of 1.3 m/s under a normal stress of 20 MPa (after Di Toro et al., 2006b). (e) Schematic sketch of the frictional evolution of granitic gneiss sheared at a slip velocity of 1.3 m/s under a normal stress of 3 MPa. Similar to Chen et al. (2017a), the evolution of powder, melt growth, and temperature with displacement is further added into our conceptual model and Stage 2 is further delimited into two regimes by the grey line. The four schematic diagrams of the slipping zone summarize how the PSD, particle volume fraction, melt distribution, microstructures and clast packing varied with frictional evolution with slip for the reference experiment LHVR0438.

Figure_01.

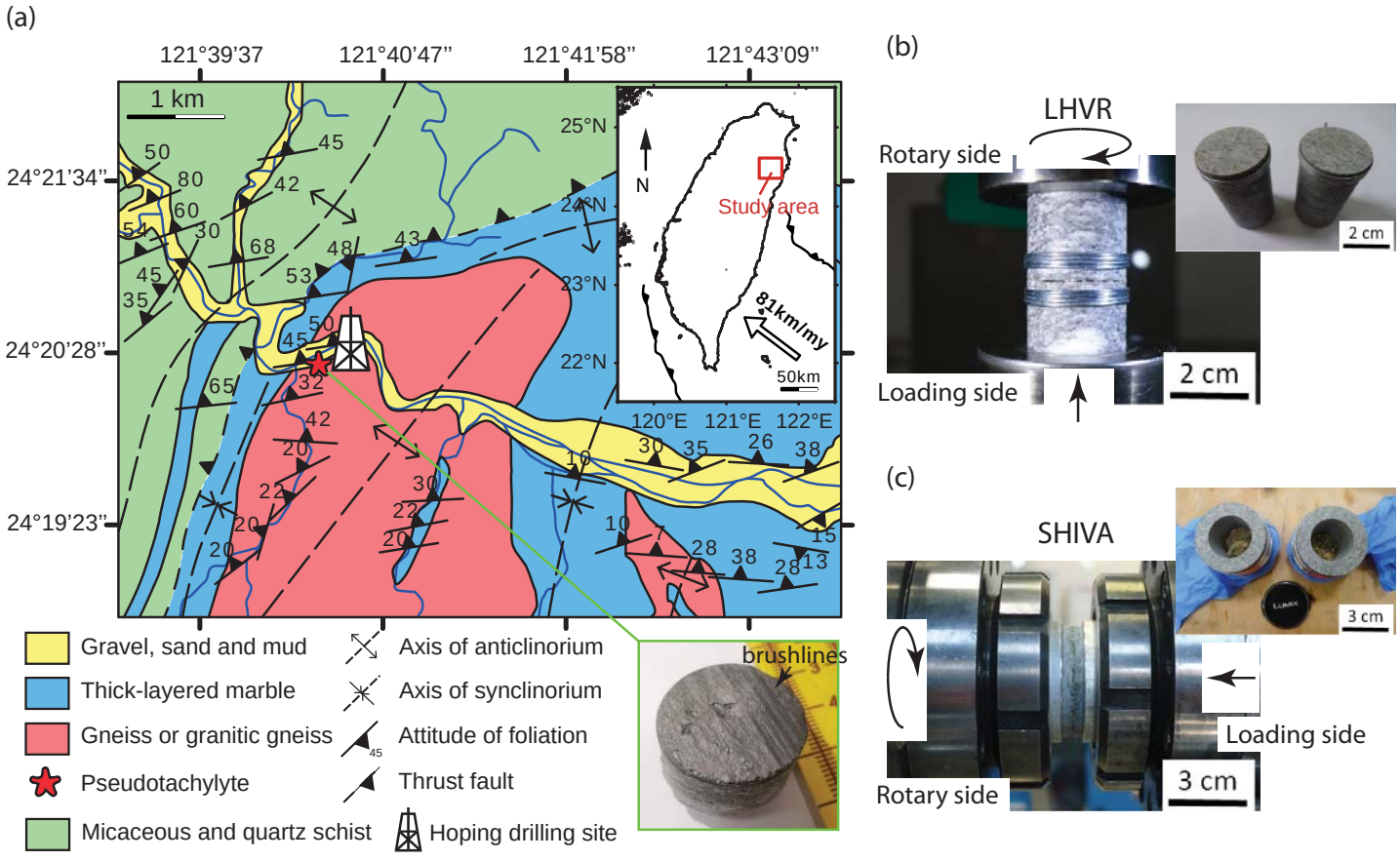
(a)
121°39'37
121°40'47"
121°41'58"
121°43'09"
24°21'34"
24°20'28"
24°19'23"
1 km
25°N
24°N
23°N
22°N
120°E
121°E
122°E
N
Study area
81km/my
50km
brushlines
Gravel, sand and mud
Thick-layered marble
Gneiss or granitic gneiss
Pseudotachylyte
Micaceous and quartz schist
Axis of anticlinorium
Axis of synclinorium
Attitude of foliation
Thrust fault
Hoping drilling site
(b)
LHVR
Rotary side
Loading side
2 cm
2 cm
(c)
SHIVA
3 cm
3 cm
Loading side
Rotary side

Figure_02.

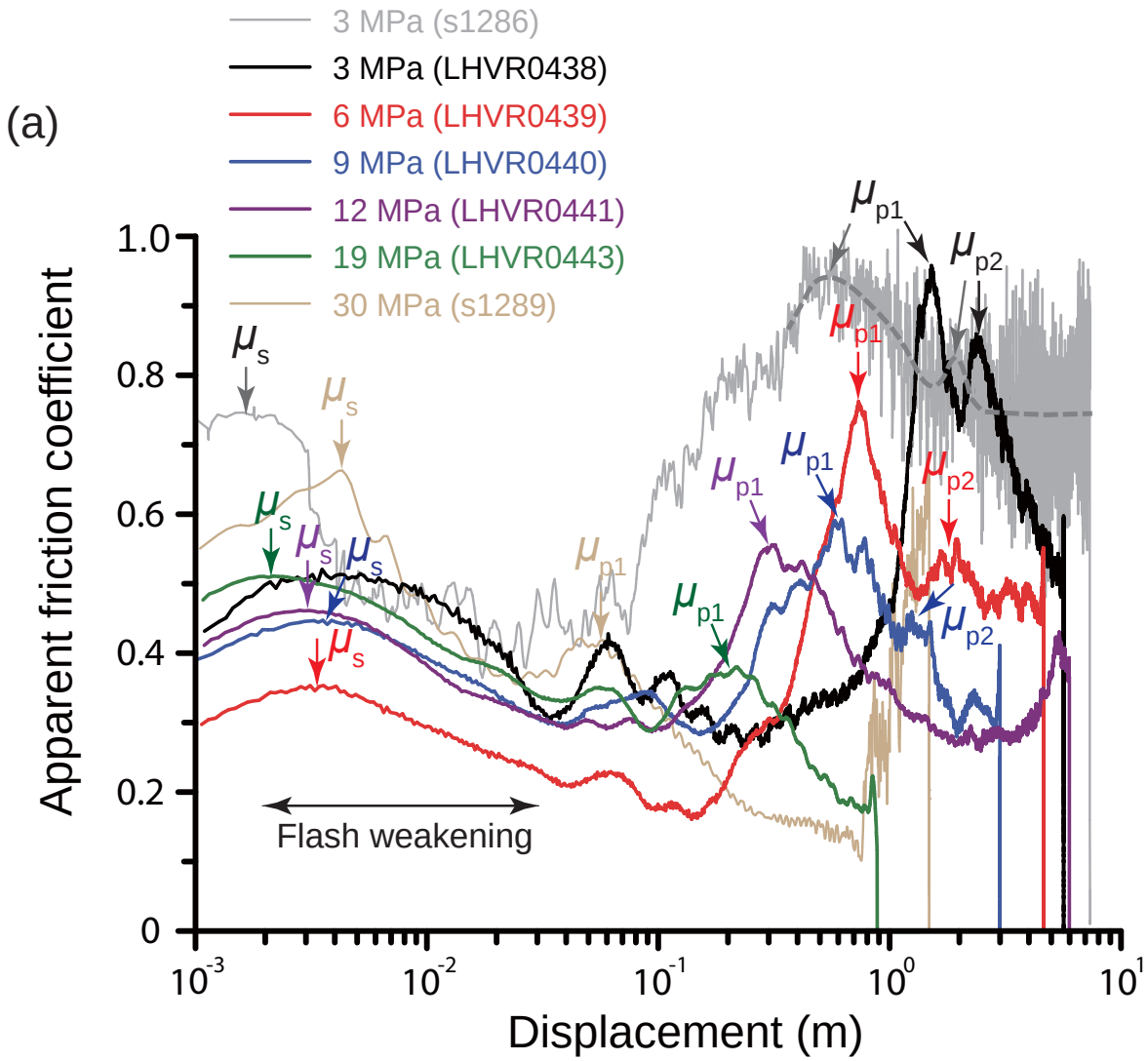
(a)
3 MPa (s1286)
3 MPa (LHVR0438)
6 MPa (LHVR0439)
9 MPa (LHVR0440)
12 MPa (LHVR0441)
19 MPa (LHVR0443)
30 MPa (s1289)
Apparent friction coefficient
Displacement (m)
Flash weakening

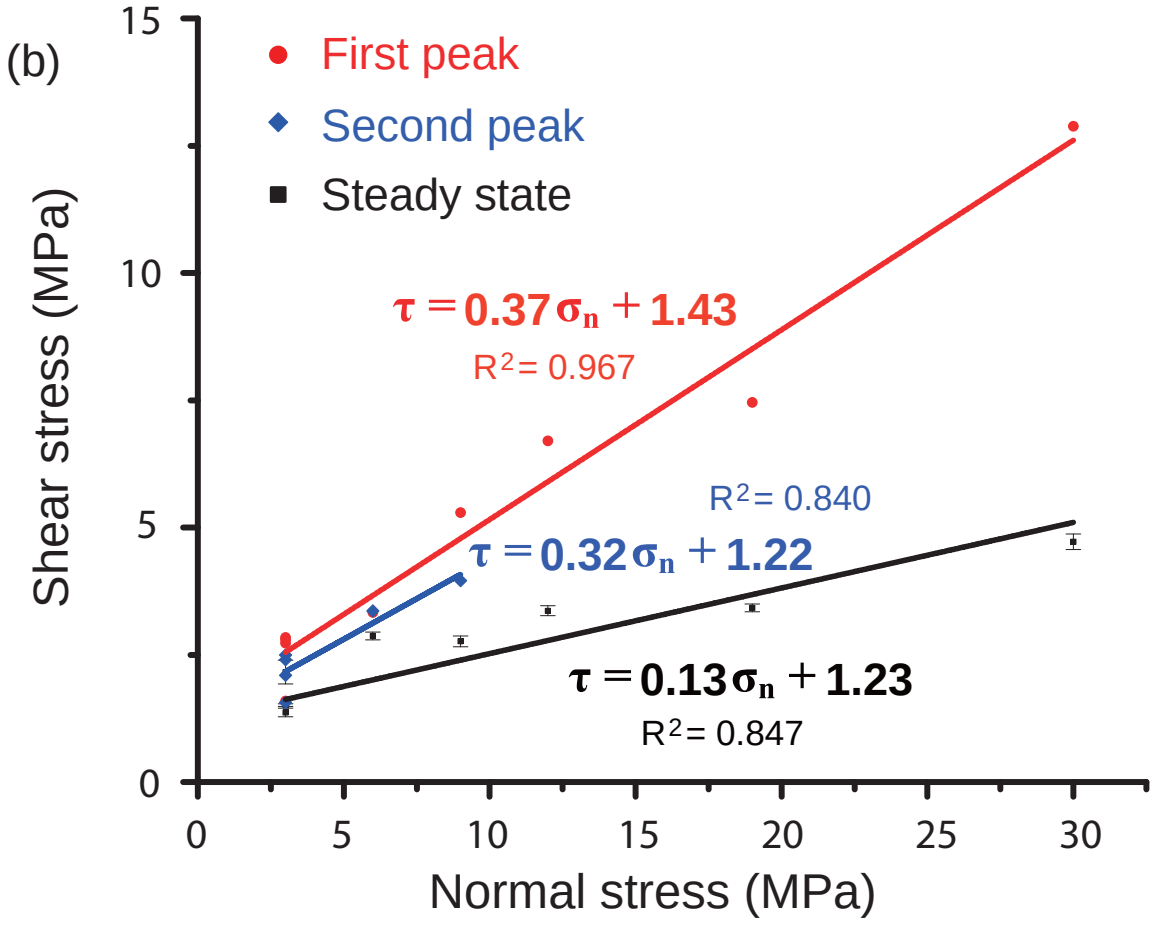
(b)
First peak
Second peak
Steady state
τ = 0.37σn + 1.43
R2 = 0.967
R2 = 0.840
τ = 0.32σn + 1.22
τ = 0.13σn + 1.23
R2 = 0.847
Shear stress (MPa)
Normal stress (MPa)

Figure_03.

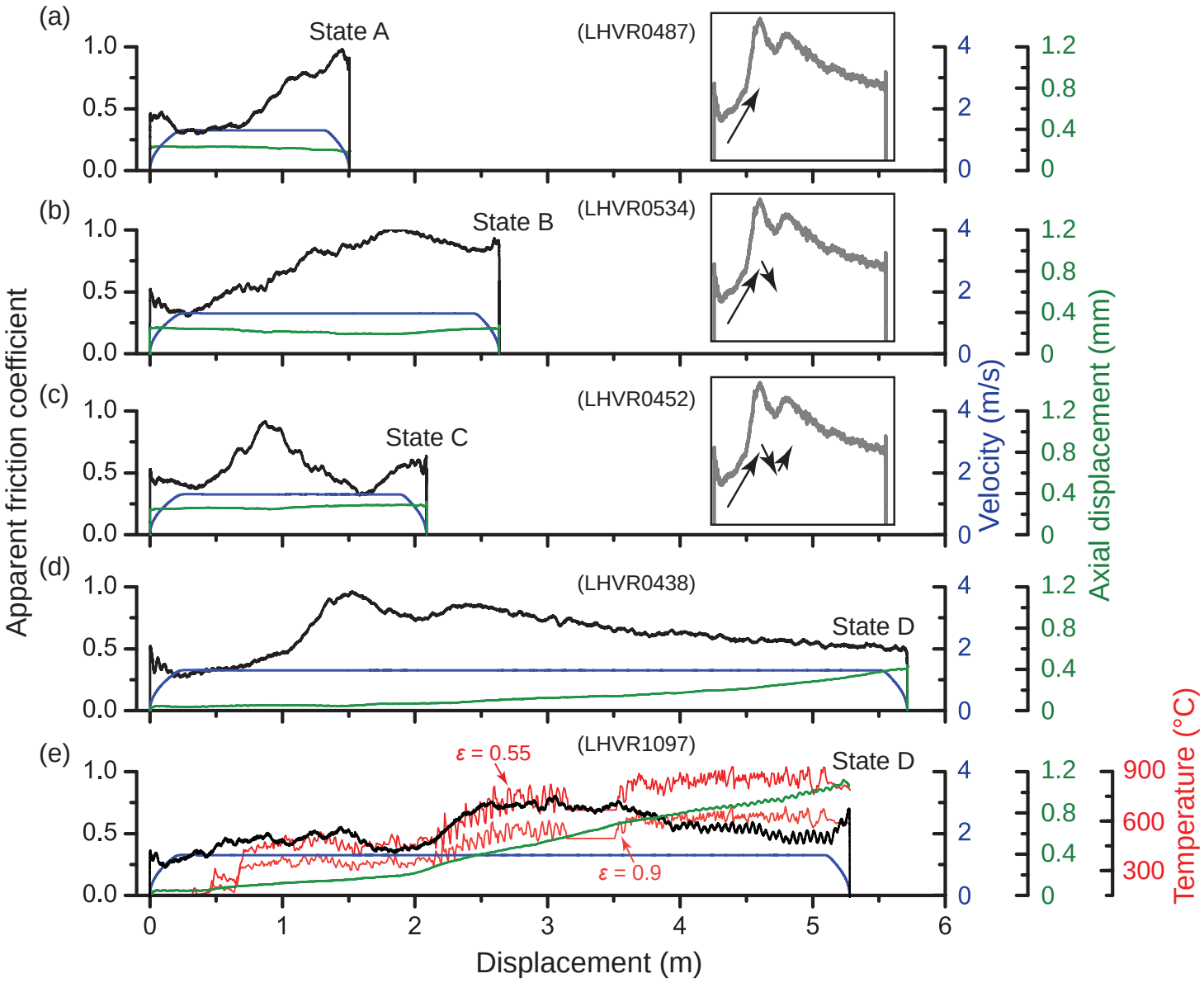
(a)
State A
(LHVR0487)
(b)
State B
(LHVR0534)
(c)
State C
(LHVR0452)
(d)
(LHVR0438)
State D
(e)
(LHVR1097)
ε = 0.55
ε = 0.9
State D
Apparent friction coefficient
Velocity (m/s)
Axial displacement (mm)
Temperature (°C)
Displacement (m)

Figure_04.

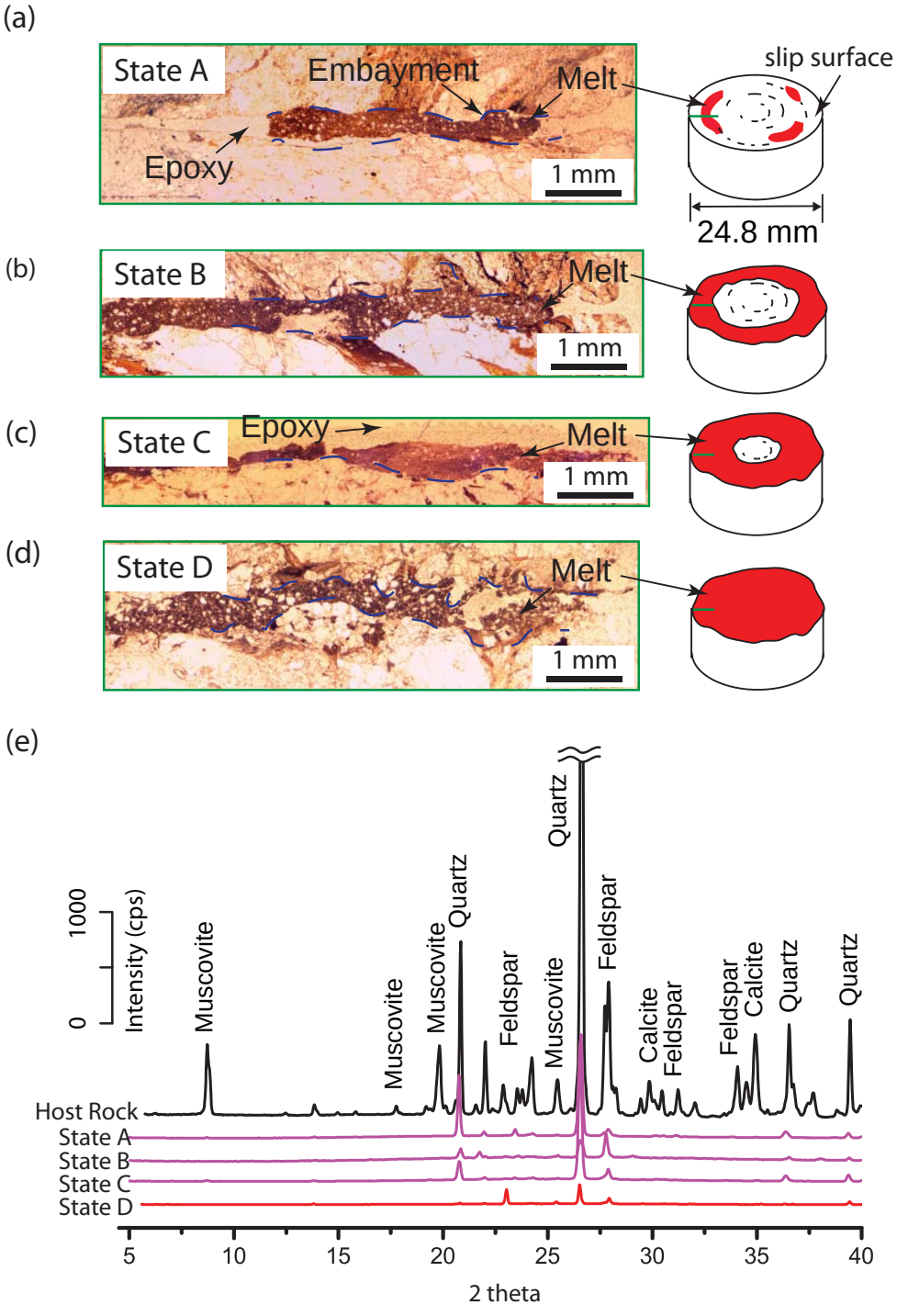
(a)
State A
Embayment
Melt
Epoxy
1 mm
slip surface
24.8 mm
(b)
State B
Melt
1 mm
(c)
State C
Epoxy
Melt
1 mm
(d)
State D
Melt
1 mm
(e)
1000
0
Intensity (cps)
Muscovite
Muscovite
Muscovite
Quartz
Quartz
Feldspar
Muscovite
Feldspar
Calcite
Feldspar
Feldspar
Calcite
Quartz
Quartz
Host Rock
State A
State B
State C
State D
5
10
15
20
25
30
35
40
2 theta

Figure_05.

(a) State A

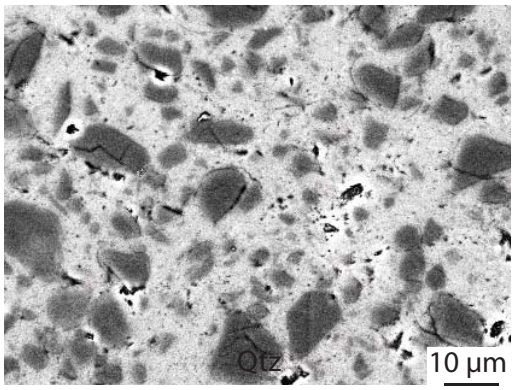

(b) State B

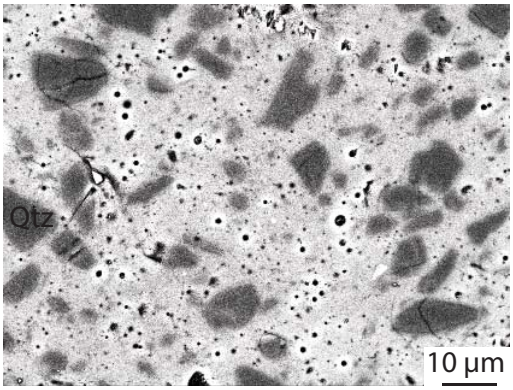

(c) State C

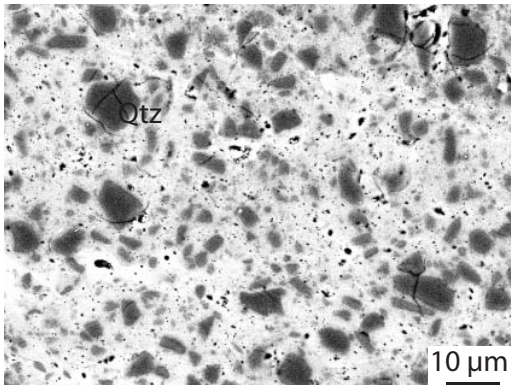

(d) State D

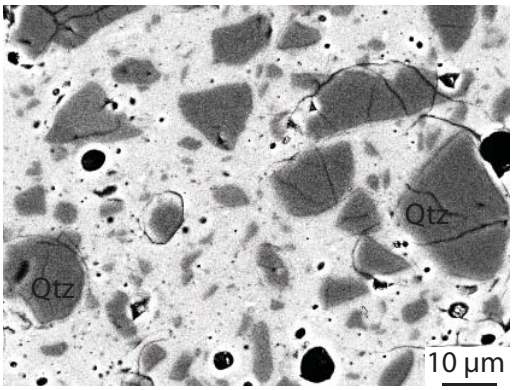

Figure_06.

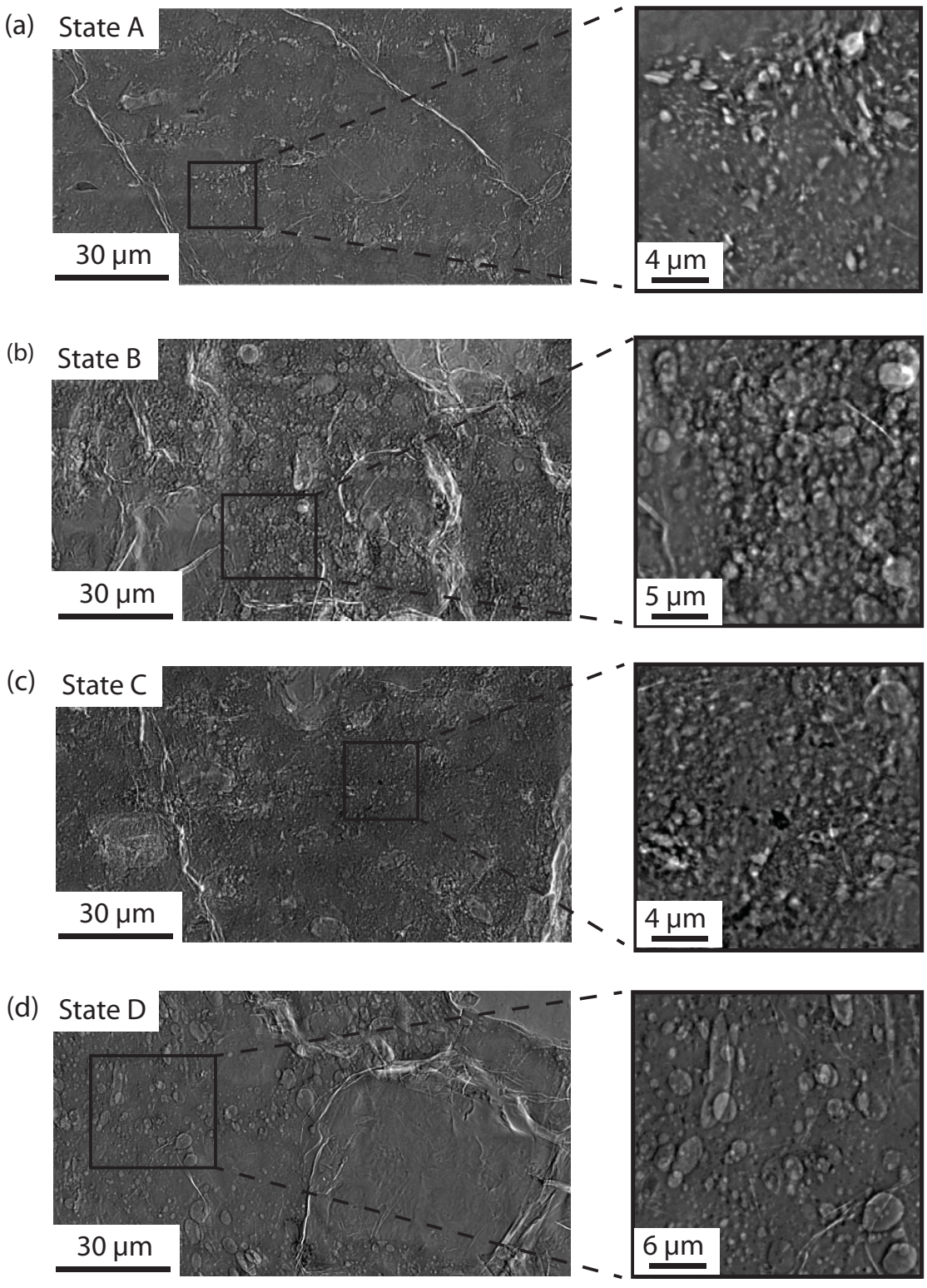
(a)
State A
30 µm
4 µm
(b)
State B
30 µm
5 µm
(c)
State C
30 µm
4 µm
(d)
State D
30 µm
6 µm

Figure_07.

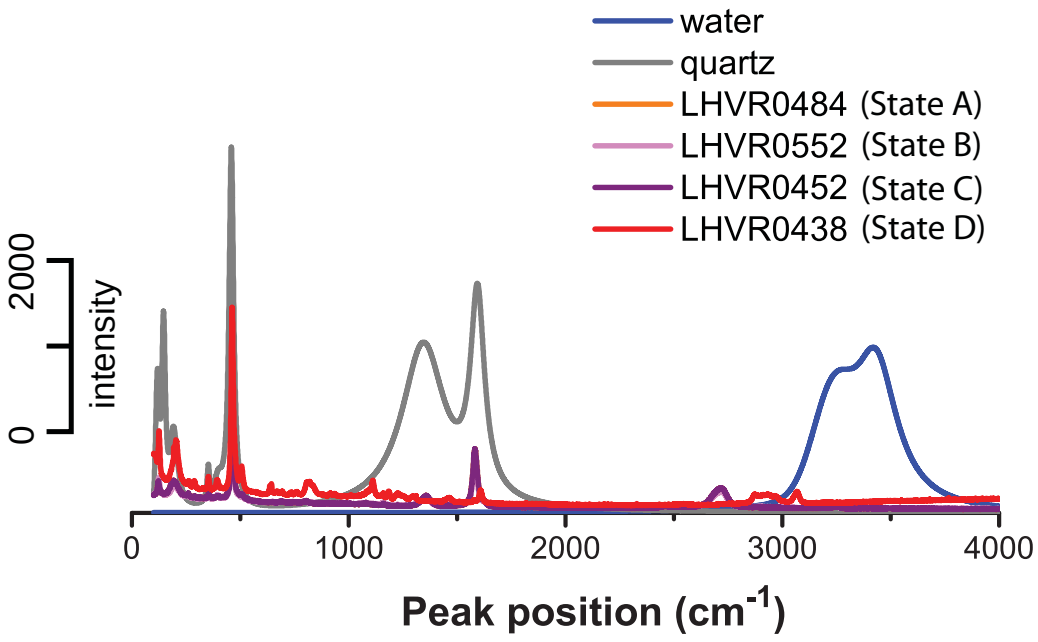
water
quartz
LHVR0484 (State A)
LHVR0552 (State B)
LHVR0452 (State C)
LHVR0438 (State D)
2000
0
intensity
0
1000
2000
3000
4000
Peak position (cm-1)

Figure_08.

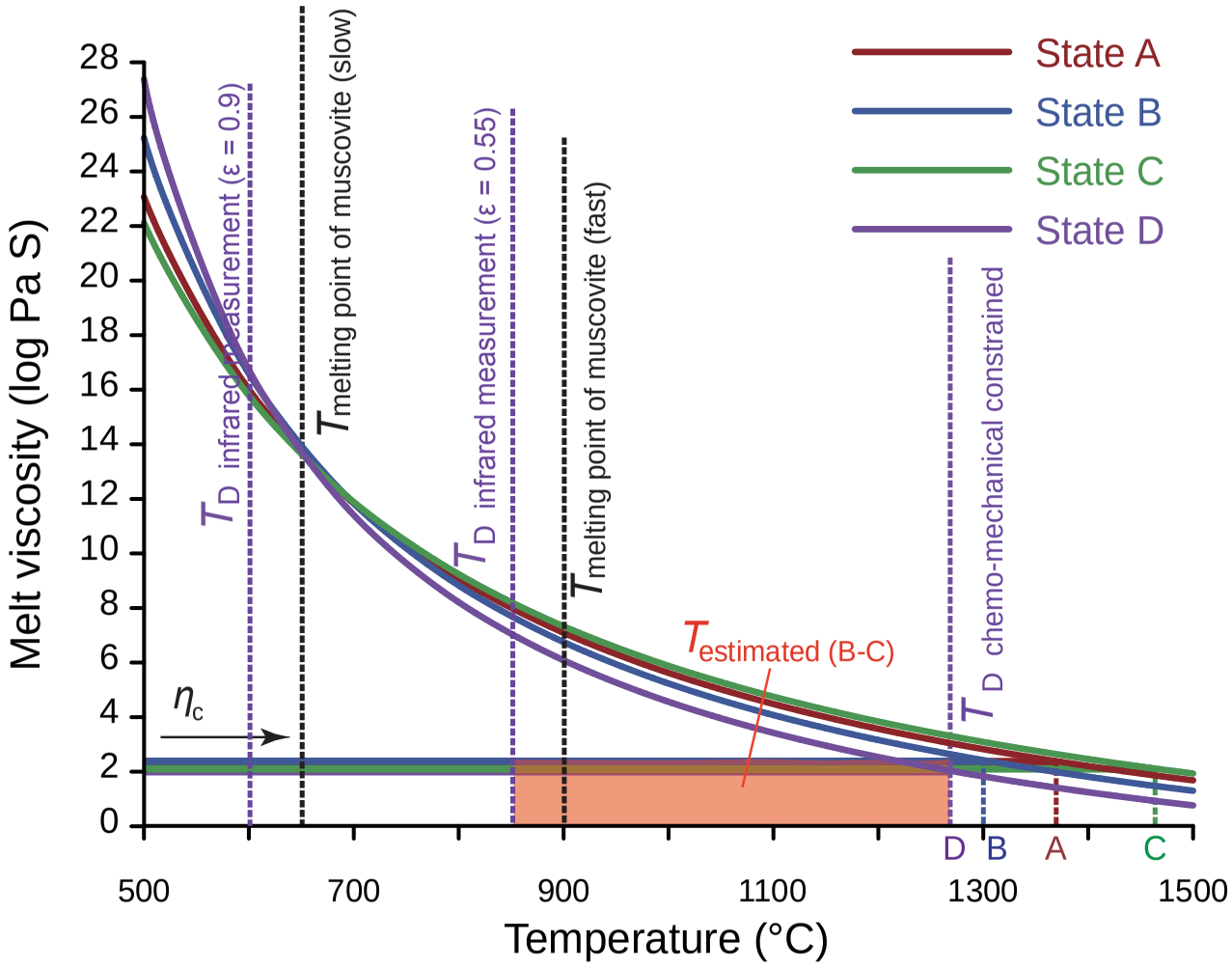
State A
State B
State C
State D
Melt viscosity (log Pa S)
28
26
24
22
20
18
16
14
12
10
8
6
4
2
0
500
700
900
1100
1300
1500
Temperature (°C)
$T_{D\ infrared\ measurement\ (\varepsilon = 0.9)}$
$T_{melting\ point\ of\ muscovite\ (slow)}$
$T_{D\ infrared\ measurement\ (\varepsilon = 0.55)}$
$T_{melting\ point\ of\ muscovite\ (fast)}$
$T_{estimated\ (B\text{-}C)}$
$T_{D\ chemo\text{-}mechanical\ constrained}$
η_c
D
B
A
C

Figure_09.

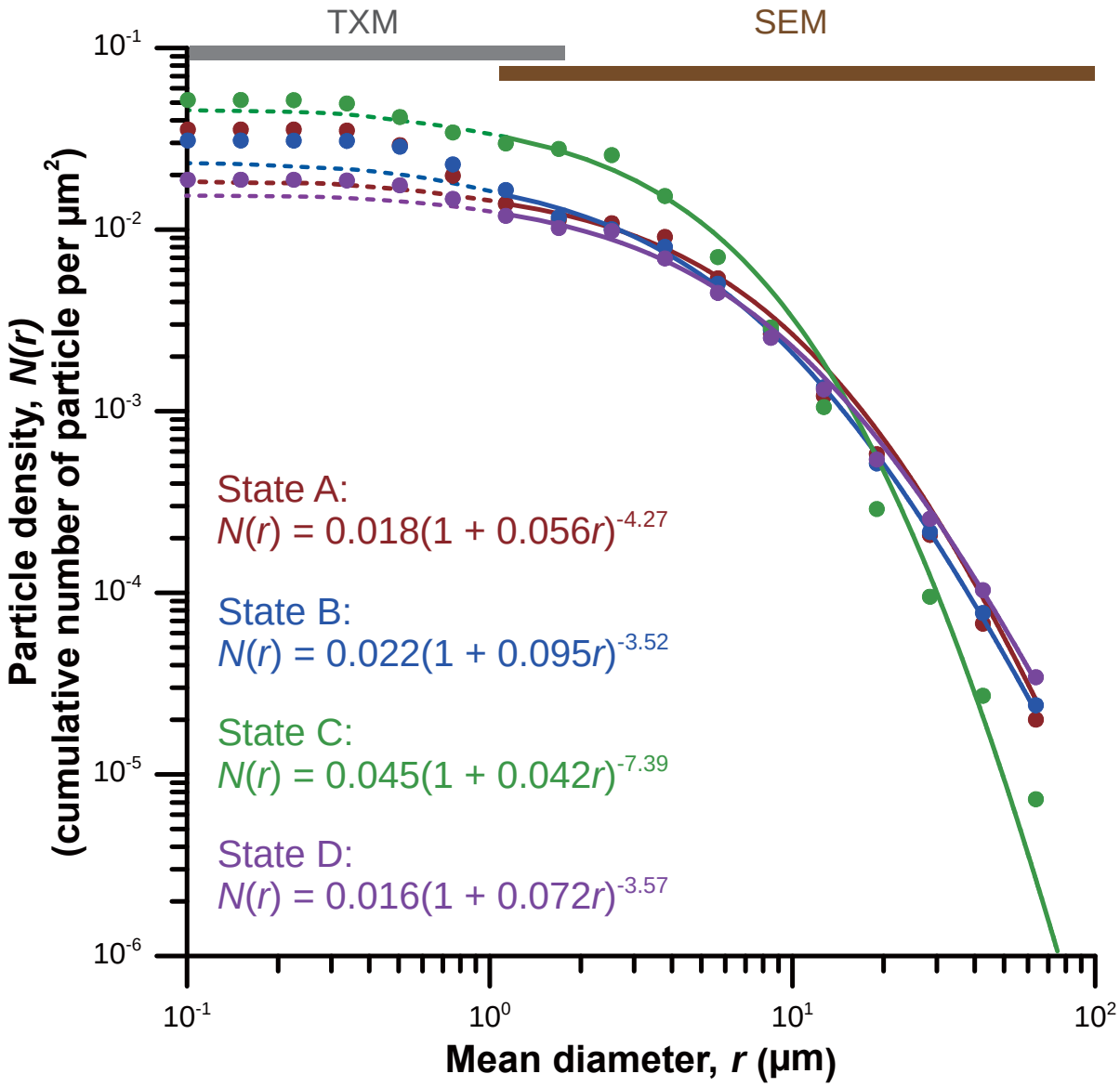
TXM
SEM
Particle density, N(r)
(cumulative number of particle per μm²)
10⁻¹
10⁻²
10⁻³
10⁻⁴
10⁻⁵
10⁻⁶
10⁻¹
10⁰
10¹
10²
Mean diameter, r (μm)
State A:
N(r) = 0.018(1 + 0.056r)^-4.27
State B:
N(r) = 0.022(1 + 0.095r)^-3.52
State C:
N(r) = 0.045(1 + 0.042r)^-7.39
State D:
N(r) = 0.016(1 + 0.072r)^-3.57

Figure_01.

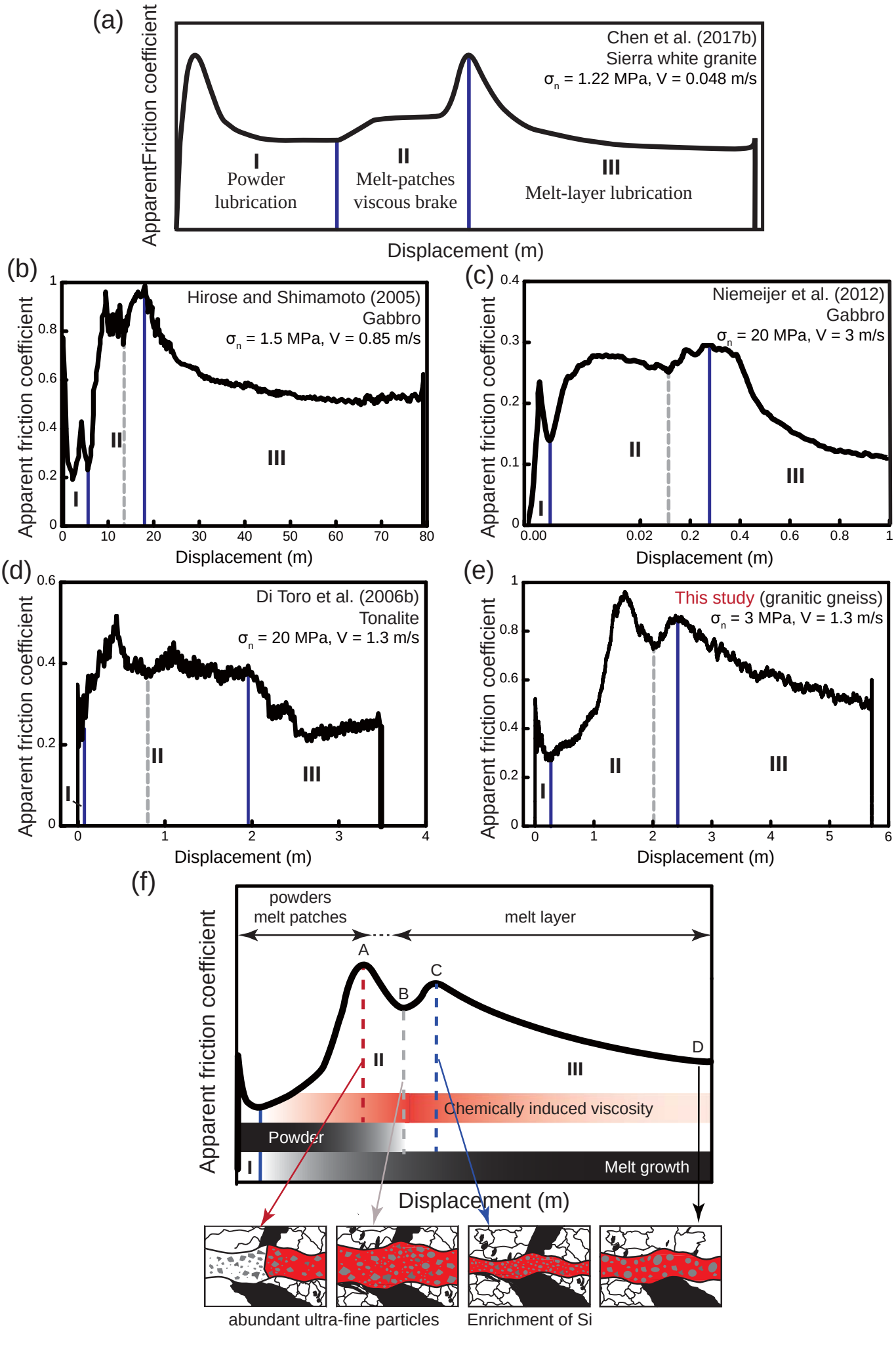
(a)
Chen et al. (2017b)
Sierra white granite
σn = 1.22 MPa, V = 0.048 m/s
Apparent Friction coefficient
I
Powder
lubrication
II
Melt-patches
viscous brake
III
Melt-layer lubrication
Displacement (m)
(b)
Hirose and Shimamoto (2005)
Gabbro
σn = 1.5 MPa, V = 0.85 m/s
Apparent friction coefficient
Displacement (m)
(c)
Niemeijer et al. (2012)
Gabbro
σn = 20 MPa, V = 3 m/s
Apparent friction coefficient
Displacement (m)
(d)
Di Toro et al. (2006b)
Tonalite
σn = 20 MPa, V = 1.3 m/s
Apparent friction coefficient
Displacement (m)
(e)
This study (granitic gneiss)
σn = 3 MPa, V = 1.3 m/s
Apparent friction coefficient
Displacement (m)
(f)
powders
melt patches
melt layer
A
B
C
D
Apparent friction coefficient
Chemically induced viscosity
Powder
Melt growth
Displacement (m)
abundant ultra-fine particles
Enrichment of Si

Table 1. Normalized average chemical composition of the granitic gneiss, glass matrix at four states, and chemically-based melt viscosity. Noted that the bulk composition of the granitic gneiss is cited from Kuo (2016) which using XRF to analyze four rock samples.

	n	Si	Al	Mg	Ca	Na	K	Ti	Fe	Mn	P	Total	Estimated melt viscosity range (Pa s)
Granitic gneiss (Kuo, 2016)	4	65.6 ± 2.42	16.2 ± 0.67	1.8 ± 0.13	2.8 ± 0.44	2.7 ± 0.05	3.8 ± 0.28	1.0 ± 0.14	5.8 ± 1.21	0.1 ± 0.00	0.2 ± 0.05	100.00	–
State A (LHVR0484)	39	58.3 ± 5.87	18.6 ± 2.64	2.1 ± 0.39	4.2 ± 0.77	2.9 ± 0.51	6.2 ± 0.82	0.6 ± 0.63	7.2 ± 1.25	–	–	100.00	$10^{8.0–3.1}$
State B (LHVR0552)	40	53.0 ± 3.47	20.4 ± 1.35	2.6 ± 0.46	4.9 ± 1.12	2.7 ± 0.85	7.1 ± 0.63	1.0 ± 0.59	8.4 ± 1.48	–	–	100.00	$10^{7.7–2.7}$
State C (LHVR0452)	39	61.3 ± 5.91	17.5 ± 2.63	2.2 ± 0.42	4.4 ± 1.22	3.0 ± 0.52	6.1 ± 0.92	0.2 ± 0.39	5.3 ± 1.20	–	–	100.00	$10^{8.2–3.3}$
State D (LHVR0438)	40	50.1 ± 3.02	17.2 ± 1.54	2.5 ± 0.3	13.5 ± 1.92	2.8 ± 0.31	6.3 ± 0.95	0.6 ± 1.34	7.0 ± 1.62	–	–	100.00	$10^{7.1–2.7}$

n, number of analyses.

Table 2. List of experiments, experimental conditions, mechanical data, and mechanically-constrained apparent viscosity.

Experiment	σ_n (MPa)	First Peak τ_{p1} (MPa)	Second peak τ_{p2} (MPa)	Average steady state τ_{ss} (MPa)	Slip velocity V (m/s)	Total slip D (m)	Acceleration/ Deceleration (m/s^2)	Melt thickness w (mm)	Apparent viscosity η_{app} (Pa S)	Clast content ϕ (%)	Apparent viscosity corrected with clasts η_c (Pa S)	Ambient condition
LHVR0484 (State A)	3	4.7	–	–	1.3	1.6	3.5	0.27	613	20	229	RH
LHVR0487 (State A)	3	2.9	–	–	1.3	1.5	3.5	–	–	–	–	RH
LHVR0534 (State B)	3	3	–	–	1.3	2.6	3.5	–	–	–	–	RH
LHVR0552 (State B)	3	3	–	–	1.3	2.7	3.5	0.33	548	18	232	RH
LHVR0452 (State C)	3	2.5	1.55	–	1.3	2.1	3.5	0.17	203	11	125	RH
LHVR0438 (State D)	3	2.8	2.5	1.5	1.3	5.7	3.5	0.23	265	20	99	RH
LHVR1097 (State D)	3	1.6	2.1	1.4	1.3	5.3	3.5	–	–	–	–	RH
LHVR0439	6	4.6	3.4	2.8	1.3	4.7	3.5	–	–	–	–	RH
LHVR0440	9	5.3	4	2.8	1.3	3	3.5	–	–	–	–	RH
LHVR0441	12	6.7	–	3.3	1.3	6	3.5	–	–	–	–	RH
LHVR0443	19	7.5	–	3.4	1.3	1.9	3.5	–	–	–	–	RH
s1286	3	3	2.4	1.6	5	7.5	6.5	–	–	–	–	Vacuum
s1289	30	12.7	–	4.7	5	1.5	6.5	–	–	–	–	RH

RH, room humidity